ELSEVIER

Nuclear Instruments and Methods in Physics Research A 449 (2000) 81–111

NUCLEAR INSTRUMENTS & METHODS IN PHYSICS RESEARCH Section A

www.elsevier.nl/locate/nima

The CLAS drift chamber system

M.D. Mestayer[a], D.S. Carman[b,c,*], B. Asavapibhop[d], F.J. Barbosa[a], P. Bonneau[a], S.B. Christo[a], G.E. Dodge[e], T. Dooling[e], W.S. Duncan[e], S.A. Dytman[f], R. Feuerbach[b], G.P. Gilfoyle[g], V. Gyurjyan[a], K.H. Hicks[c], R.S. Hicks[d], C.E. Hyde-Wright[e], G. Jacobs[a], A. Klein[e], F.J. Klein[a], M.V. Kossov[j], S.E. Kuhn[e], R.A. Magahiz[b,1], R.W. Major[g], C. Martin[e], T. McGuckin[e], J. McNabb[b], R.A. Miskimen[d], J.A. Mueller[f], B.B. Niczyporuk[a], J. O'Meara[a], L.M. Qin[e], B.A. Raue[e,h], J. Robb[a], F. Roudot[k], R.A. Schumacher[b], D.J. Tedeschi[f,i], R.A. Thompson[f], D. Tilles[a], W. Tuzel[a,2], K. VanSyoc[e], M.F. Vineyard[g], L.B. Weinstein[e], G.R. Wilkin[b], A. Yegneswaran[a], J. Yun[e]

[a] *Jefferson Laboratory, Newport News, VA 23606, USA*
[b] *Carnegie Mellon University, Pittsburgh, PA 15213, USA*
[c] *Ohio University, Athens, OH 45701, USA*
[d] *University of Massachusetts, Amherst, MA 01003, USA*
[e] *Old Dominion University, Norfolk, VA 23529, USA*
[f] *University of Pittsburgh, Pittsburgh, PA 15260, USA*
[g] *University of Richmond, Richmond, VA 23173, USA*
[h] *Florida International University, Miami, FL 33199, USA*
[i] *University of South Carolina, Columbia, SC 29208, USA*
[j] *Institute of Theoretical and Experimental Physics, Moscow 117259, Russia*
[k] *CEA/Saclay, DAPNIA-SPhN, F-91191 Gif-sur-Yvette Cedex, France*

Received 12 May 1999; received in revised form 24 November 1999; accepted 29 November 1999

Abstract

Experimental Hall B at Jefferson Laboratory houses the CEBAF Large Acceptance Spectrometer, the magnetic field of which is produced by a superconducting toroid. The six coils of this toroid divide the detector azimuthally into six sectors, each of which contains three large multi-layer drift chambers for tracking charged particles produced from a fixed target on the toroidal axis. Within the 18 drift chambers are a total of 35,148 individually instrumented hexagonal drift cells. The novel geometry of these chambers provides for good tracking resolution and efficiency, along with large acceptance. The design and construction challenges posed by these large-scale detectors are described, and detailed results are presented from in-beam measurements.

* Corresponding author. Correspondence address: Ohio University, Department of Physics, Athens, Ohio 45701, USA. Tel.: + 1-740-593-2964; fax: + 1-740-593-1436.

E-mail address: carman@ohiou.edu (D.S. Carman).

[1] Present address: Syncsort Inc, Woodcliff Lake, NJ 07695, USA.

[2] Present address: Los Alamos National Laboratory, Los Alamos, NM 87545, USA.

0168-9002/00/$ - see front matter
PII: S0168-9002(00)00151-0

PACS: 29.40.Cs; 29.40.Gx

Keywords: CLAS; Drift chambers; Tracking system

1. Tracking system design

The Continuous Electron Beam Accelerator Facility (CEBAF) at Jefferson Laboratory is based on a recirculating multi-GeV electron linear accelerator. Located in Experimental Hall B of this facility is the CEBAF Large Acceptance Spectrometer (CLAS), a detector for use with electron and tagged-photon beams. CLAS is constructed around six iron-free superconducting coils that generate a toroidal magnetic field. The particle detection system consists of drift chambers to determine charged-particle trajectories, Cherenkov detectors for electron/pion separation, scintillation counters for flight-time measurements, and calorimeters to identify electrons and high-energy neutral particles. Overviews of the CLAS subsystems and geometry may be found in the CEBAF Hall B Conceptual Design Report [1]. A schematic three-dimensional view of the detector is shown in Fig. 1. Figs. 2 and 3 represent horizontal and vertical cuts through the detector, respectively.

CLAS was designed to track charged particles emerging from the target with momenta greater than 200 MeV/c over the polar angle range from 8° to 142°, while covering up to 80% of the azimuth. In order to achieve this, it is necessary to reconstruct the trajectories of all charged particles that do not strike the cryostat of the toroidal magnet. All non-active parts of the drift-chamber structure are required to reside in the "shadow" of the torus cryostat as viewed by rays from the target, imposing tight space constraints. Track resolution goals for 1 GeV/c charged particles were $\delta p/p \leq 0.5\%$ for the reconstructed momentum, and $\delta\theta$, $\delta\phi \leq$ 2 mrad for the reconstructed scattering angles. To achieve these goals, the tracks had to be measured at three locations along their trajectories to an accuracy of 100 μm in the bend plane of the magnetic field and 1 mm perpendicular to the bend plane. Furthermore, in order to reduce multiple scattering, the total amount of material in the tracking region of the detector was required to be less than 1% of a radiation length.

The CLAS toroidal magnet bends charged particles towards or away from the beam axis but leaves the azimuthal angle essentially unchanged. The $\int \boldsymbol{B} \times d\boldsymbol{l}$ varies from 2 T m for high momentum tracks at the most forward angles to about 0.5 T m for tracks beyond 90°. The magnet coils naturally separate the detector into six independent tracking areas or "sectors", since a particle that leaves the target and enters a sector stays within that sector. To simplify detector design and construction, 18 separate drift chambers were built and located at three radial locations in each of the six sectors. These radial locations are referred to as "Regions". The "Region One" chambers (R1) surround the target in an area of low magnetic field, the "Region Two" chambers (R2) are somewhat larger and are situated between the magnet coils in

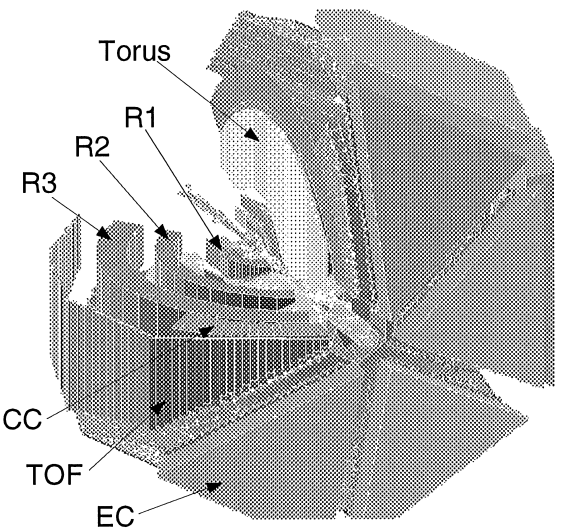

Fig. 1. Three dimensional representation of CLAS with a portion of the system cut away to highlight the elements of the detector system along with their geometries and relative positions. The detector support structures are not shown.

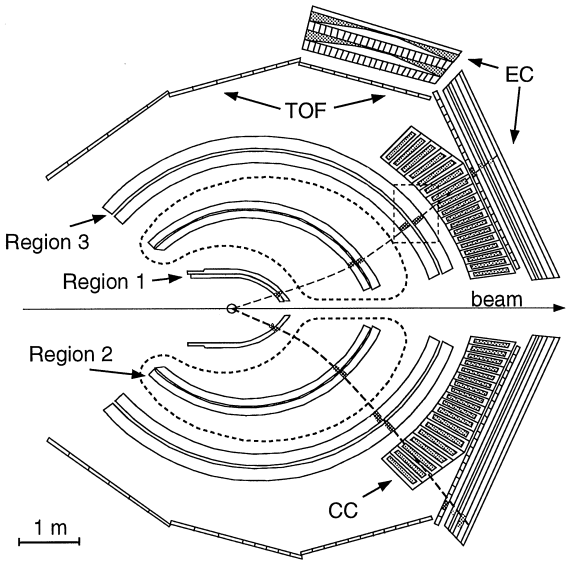

Fig. 2. Horizontal cut through the CLAS detector at beam line elevation showing two charged particles traversing the drift chambers in opposite sectors. Outside of R3 are the remainder of the CLASS detectors including Cherenkov counter (CC), scintillators (TOF), and calorimeters (EC). The dotted lines show the projection of the torus coils on the sector mid-plane. Fig 4 shows an enlargement of the boxed area.

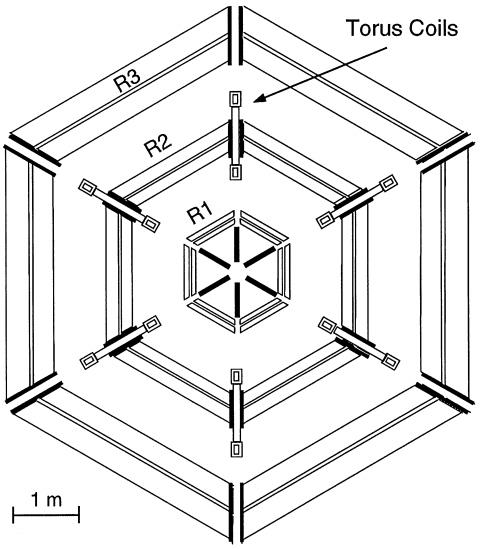

Fig. 3. Vertical cut through the drift chambers transverse to the beam line at the target location showing the geometric relationship of the detectors.

an area of high field near the point of maximum track sagitta, and the "Region Three" chambers (R3) are the largest devices, radially located outside of the magnet coils.

To optimally fill the wedge-shaped volume between the torus coils, the chamber bodies were designed to support wires running between two endplates, each parallel to its neighboring coil plane, and thus tilted at 60° with respect to each other. This design provides maximum sensitivity to track momenta since the wire direction is approximately perpendicular to the bend plane of the curved trajectories. The wire midpoints are arranged in "layers" of concentric circles. For pattern recognition and tracking redundancy, the wire layers are grouped into two "superlayers", one axial to the magnetic field, and the other tilted at a 6° stereo angle around the radius of each layer to provide azimuthal information. Each superlayer nominally consists of six layers of drift cells as shown in Fig. 4.

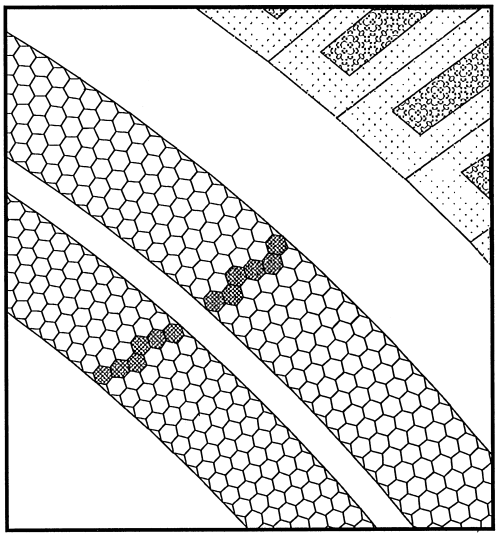

Fig. 4. Representation of portion of an R3 sector showing the layout of its two superlayers. The sense wires are at the center of each hexagon and the field wires are at the vertices. The perimeters of the hexagons are shown to outline each cell. Not shown are the guard wires that surround each superlayer. In this view, projected on the mid-plane of the sector, a passing charged particle is shown by the highlighted drift cells that have fired. Beyond the drift chamber, in the upper right corner, the edge of a Cherenkov detector is shown.

The wire positions are shifted by half the nominal spacing in successive layers. This "brick-wall" pattern of wires in neighboring layers, with a repeating pattern of two field-wire layers and one sense-wire layer, results in a quasi-hexagonal pattern with six field wires surrounding one sense wire. The cell size increases uniformly with increasing radial distance from the target. A layer of guard wires surrounds the perimeter of each superlayer with high-voltage potential adjusted to reproduce the electric-field configuration given by an infinite grid of hexagonal cells, i.e. the electric field at the sense wire surface is approximately the same for all sense wires, independent of wire-layer number [2].

The hexagonal configuration was chosen for several reasons. In a typical CLAS data sample, charged-particle tracks traverse the chambers at widely varying angles. In contrast to jet cells that are optimized for tracks with a particular direction, hexagonal cells offer a reasonable approximation to the ideal circular cell in which the drift time to drift distance relation is independent of entrance angle. In addition, the brick-wall layout allows for a more straightforward resolution of the side of the sense wire that the track was located on. Of equal importance, the hexagonal layout reduces the electrostatic forces on the wires, allowing for lower wire tensions, which in turn allows for the use of thinner endplates. Thin endplates are required to keep material from projecting out of the shadow of the torus cryostats and thus reducing the acceptance of the spectrometer.

2. Chamber construction

2.1. Construction overview

The three chamber Regions share many of the same basic design elements. Each is made up of six identical wedge-shaped sectors constructed from a pair of long wire-supporting endplates that bear both the load of the wire tensions and the weight of all associated hardware. A representative chamber sector is shown in Fig. 5. The wire tension load was handled differently in each Region; in R1 the load was balanced by the wire tension in neighboring sectors after the six chambers were integrated into

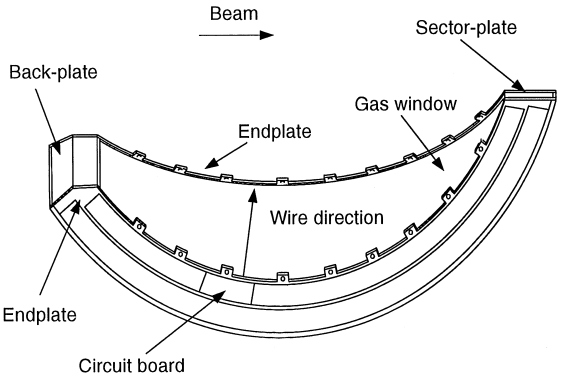

Fig. 5. Schematic representation of a typical drift-chamber sector (here a R3 sector) highlighting some of the common hardware pieces used by each.

a single unit (see Section 3.1), in R2 the load was supported by the torus cryostat, and in R3 the wire tension was offset by compression in a carbon-fiber outer shell and in a set of five carbon-fiber posts that were part of the chamber construction. At the upstream end of each sector, a thick "back-plate" was employed to maintain the relative alignment of the endplates, to stiffen the sector against bending moments, and to provide a place to attach gas seals and fittings. At the downstream end of each sector, the endplates were connected together via a small joining piece called the "sector-plate". The hardware fabrication and placement was of critical importance to the dimensional accuracy of the chambers.

Each endplate contains thousands of accurately positioned holes into which the wire-fixture assemblies were placed. The sense, field, and guard wires in each sector were strung between pairs of wire "feedthroughs". As the endplates of each chamber faced each other at a 60° angle, the wires had to bend 30° at each endplate. This was accomplished by means of a large radius stainless-steel insert at the tip of each feedthrough known as a "trumpet". This trumpet was fitted into an injection-molded Noryl plastic feedthrough in the case of R1 and R3, or directly into the endplate for R2. All wires are held in place using gold-plated copper crimp pins. Low-outgassing epoxy is employed to ensure a gas seal around the feedthroughs and crimp pins. The trumpet assemblies are shown in Figs. 7, 8, and 9 for R1, R2, and R3, respectively.

2.2. Wire and gas choice

To limit wire tensions and operating voltages meant that the wire diameter had to be minimized. The sense wire for all chambers, supplied by the Luma Sweden Company, consists of 20-μm diameter gold-plated tungsten, the smallest practical choice. Tungsten was chosen because of its durability, and the gold-plating of the wires, amounting to a thickness of 0.127 μm, ensures chemical inertness as well as a smooth surface finish. The expected electronics gain and thresholds dictated that the gas gain be a few times 10^4. Under this condition, the electric field at the surface of the sense wires is ≈ 280 kV/cm. The field-wire diameter was chosen to ensure that the electric field at their surface remained below 20 kV/cm to minimize conditions causing cathode deposits [3,4]. Since there are roughly twice as many field as sense wires, this required that the diameter of the field wires be about seven times the diameter of the sense wire. The field wire for all chambers consists of 140-μm diameter gold-plated aluminum 5056 alloy from the California Fine Wire Company. Aluminum was chosen because it has the longest radiation length of any practical wire material and thus minimizes multiple scattering. Additionally, the low density of aluminum means that the field wires could be strung at lower tension than a more dense wire, with minimal gravitational sag. This minimizes the forces on the endplates.

The main requirements for the chamber gas were that it should have reasonably low multiple scattering, allow for reasonable gas gains, have short collection times in order to reduce the random background expected from Møller electrons and target-generated X-rays, and be inexpensive because of the large volume of the chambers. The initial choice of chamber gas was a 50% argon–50% ethane mixture. However, safety concerns prompted a search for a non-flammable gas mixture. Additional concerns about small gas leaks and the proximity of many photomultiplier tubes argued against helium mixtures. Ultimately, a 90% argon–10% CO_2 mixture was employed for several reasons: the gas has a fairly high saturated drift velocity (> 4 cm/μs), and it has an operating voltage plateau of several hundred volts before breakdown occurs. A 95%/5% mixture achieves velocity saturation at even lower values of the electric field but has an excessively short voltage plateau due to lack of quenching. The 90%/10% mixture provides good efficiency, adequate resolution, and reasonable collection times.

2.3. Construction materials

Due to the complex geometry of CLAS and the difficulty of removing and repairing drift chambers, it was crucial to minimize chamber aging. Care was taken to ensure that all materials in contact with the gas volume were clean and "chamber safe" as defined in Ref. [3]. All construction was carried out in Class-10000 or better clean rooms.

The drift-chamber frames are made primarily of aluminum (R1), fiberglass (R2), or steel-clad structural foam (R3). The aluminum and steel endplates were manufactured with machine oils and were subsequently cleaned with Micro-laboratory detergent from the Cole-Parmer Instrument Company. The fiberglass endplates were machined without any lubricating oils. Immediately prior to chamber assembly all endplates were sequentially cleaned with detergent, deionized water, and alcohol, and then blown dry with pure nitrogen gas. The wire feedthroughs, trumpets, and crimp pins were cleaned in an ultrasonic bath with detergent and then rinsed in a second ultrasonic bath with deionized water.

During construction three different types of epoxy were used in areas exposed to the chamber gas. Shell Epon resin 826 mixed with Versamid 140, and Scotchweld varieties 210 and 2216 were employed. These mixtures have been studied extensively and found not to outgas significantly [5].

The on-chamber gas tubing employed is mainly stainless steel, with some nylon tubing included for gas manifolds. Special care was taken during all steps of construction and testing to ensure that no oils or silicones contacted any of the chamber materials.

2.4. Chamber wire stringing

With nearly 130,000 wires to be threaded through the chambers and only 2 years for

construction, it was important to minimize the time required to string each wire. All chambers were strung with the wires running vertically. The stringing technique involved attaching a small steel needle to the wire before threading it through the feedthrough in the upper endplate. The wire was then de-spooled and gravity acted to bring the wire close to the feedthrough in the lower endplate. A small magnet was then used to pull the needle and wire through the lower feedthrough. After the upper crimp pin was attached and remaining slack in the wire was removed, the lower crimp pin was slid over the wire and stringing weights were attached to set the proper tension. The lower crimp pin was then attached, completing the process.

Wires that wrapped around each other while being threaded through the chamber were a major contribution to stringing inefficiency. To avoid the wrapping problem, a machine was built to spool the wire through the chambers at a fast and smooth rate. Another important development was the design of a crimp pin that accepted both the tungsten and aluminum wire types. Using a thick-walled copper pin ensured a good crimp through a range of gap settings [6]. This eliminated the need to use separate crimping tools, each requiring frequent calibrations. This was possible because the wire position was determined by the radius of the trumpet at the end of the feedthrough inside of the chamber, and not by the concentricity of the pin, feedthrough, and endplate-hole diameters. As a result, the average time to string a wire was less than 4 min.

2.5. Region-one construction

The R1 chambers were designed and constructed through a collaboration of Carnegie Mellon University, the University of Pittsburgh, and the University of Massachusetts. These detectors constitute the innermost of the three nested drift-chamber packages surrounding the target in the spectrometer [7]. The R1 detectors track all charged particles prior to their entry into the magnetic field of the CLAS torus.

R1 consists of six identical sectors integrated into a single unit. Each sector consists of 1296 hexagonal drift cells ranging in diameter from 15 to 17 mm, with all wires located within 1 m of the primary beam. Each sector consists of two superlayers, the stereo layer at smaller radius, and the axial layer at larger radius. This arrangement, which is opposite to the outer two Regions, was necessitated by space constraints within the torus. While each R2 and R3 sector consists of 12 layers of sense wires, the limited space within the torus allowed for only 10 layers in each R1 sector. The final R1 design included 6 axial layers and four stereo layers. Space constraints at the most backward angles spanned by R1 required a reduction in the number of axial wire layers from 6 to 3, as can be seen in Fig. 6. Also the layer contour changes shape from circular to straight for polar angles greater than 90°.

Sense wires are shifted by ± 300 μm from the nominal position from one wire layer to the next. This "mini-stagger" feature helps to resolve the track path for those tracks that run nearly parallel to a series of drift cells. The size of the stagger was chosen such that the induced drift time differences could be resolved easily. R2 and R3 did not stagger sense wires in this way.

Fig. 6 shows a schematic of how the wire-supporting endplates are captured within the torus cryostat, as well as some of the detector support structures. To protect the chambers from charged

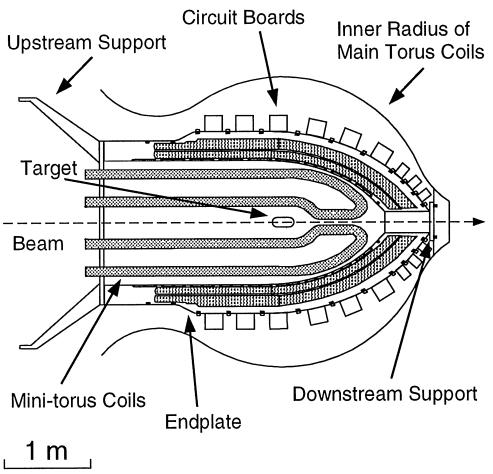

Fig. 6. Schematic side-view cross section of R1 highlighting the locations of the main torus, target, and detector supports. The shaded areas along the endplates correspond to the wire hole patterns.

electromagnetic background emerging from the target, a small normal-conducting "mini-torus" magnet is located inside of R1 during standard electron-beam operation. The integral magnetic field of the mini-torus is about 5% that of the main torus.

The shapes of the outer main torus and the inner mini-torus limited the amount of space available for the R1 chambers, along with their associated on-board electronics, cables, and support hardware. Fig. 7 shows a projection of a portion of the detector near 90° to highlight how the wire-support hardware, circuit boards, and cables were arranged to fit within the shadow region of the torus cryostats.

The 228-cm long wire-supporting endplates are made of 8-mm thick, 50-cm wide Alcoa Alca-Plus cast tooling plate, a non-magnetic alloy reputed to have low internal stresses, and, therefore, thought to have minimal distortion after the hole pattern was drilled. Holes for the wire feedthroughs and assembly hardware were drilled with a 4-mm diameter and an absolute position tolerance of 130 μm. Measurements of the finished plates showed systematic positional distortions near 100 μm, some due to the manufacturing, and some of which were consistent with few-degree temperature differences between manufacturing and measuring [8].

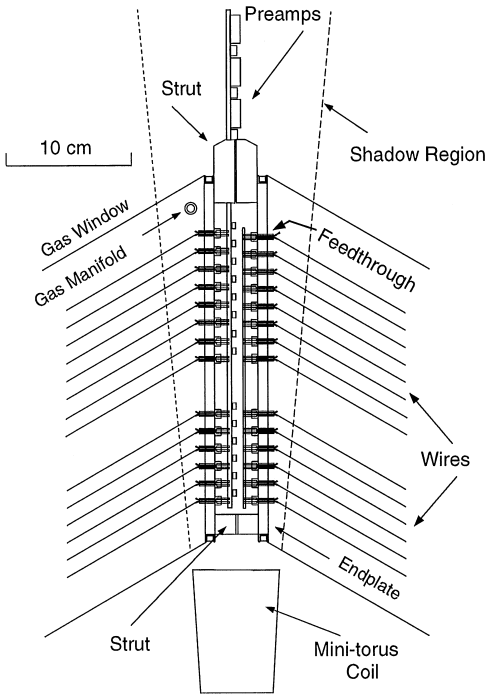

Fig. 7. Endplates and other components from neighboring R1 sectors seen in projection. Feedthroughs, crimp pins, and circuit boards for pairs of sectors, along with the strut fixtures, had to fit within 3.5 cm of space to be contained within the shadow of the torus magnet.

Single sectors are built out of endplate pairs that support most of the R1 mechanical loads. During sector construction, the endplate spacing was controlled at 22 points along their inner and outer perimeters to an accuracy of 25 μm using temporary 1.59-cm diameter aluminum posts. Struts machined to precise angles and affixed to the edges of the endplates supported the posts, and later formed the mating surfaces for joining one sector to the next. A ball-and-socket mechanism allowed accurate coupling of the posts to the sectors while later allowing smooth and simple removal of the posts upon integration of the finished sectors into a single unit. The lengths of the posts and struts defined the geometry of the sectors to 50 μm precision.

Deciding where to support the thin sector endplates, in view of the heavy loads placed upon them, presented a complex mechanical problem that was solved using two approaches. First, finite-element modeling of the endplates was used to understand the distribution of forces and deflections under the loads of the wires and of gravity [9]. This allowed for proper selection of the number, spacing, and position of the support posts. Second, a full-scale prototype of the detector was built to test and improve the mechanical design, as well as to practice the assembly procedure. Thick piano wires modeled groups of about 200 sense and field wires, and lead weights modeled the electronics and cables. Fine wires were strung to monitor tension changes in response to various steps in the assembly and installation procedure.

The endplate pairs each connect to thick aluminum back-plates, which in turn connect to a large six-sided annular support ring that also serves to align the six sectors. After installation, three support legs anchor the support ring to the upstream portion of the cryostat, constraining the position of the chamber along the central beam axis. At the

downstream end of each sector, the sector-plates connect to a small six-sided cylindrical pipe that ultimately anchors onto a set of dowel pins on the cryostat.

Fig. 7 highlights the hardware pieces described in the text including the struts and wire feedthroughs. The 4.8-mm length of the plastic feedthroughs provide separation between each trumpet at high voltage and the grounded endplate. Not shown are the custom-built polyethylene U-channels used to attach the 15-μm aluminized-nylon gas windows to the inner and outer edges of the endplates. For this purpose the glue seals were made with Scotchweld 2216 epoxy. A 0.64-cm diameter stainless-steel gas input line runs longitudinally along the endplate to inject gas into the downstream end of each sector. Another line is used to exhaust gas from the upstream end of the detector.

Most of the challenges associated with the detector construction came about because the endplates are not rigid. This lack of stiffness led to two important effects that required detailed consideration [10]. First, the forces applied by the wires caused the endplates to deflect by up to 1 mm. These deflections, which changed the tensions in some wires by over 50% of their strung value, were compensated for by pre-tensioning the sectors prior to stringing. That is, 67 heavy steel wires were installed in order to deform the endplates prior to stringing, using effective mass loads between 2 and 14 kg. For each of the six sectors, 3435 field and guard wires were strung at a nominal tension of 100 g, and 1296 sense wires were strung at a nominal tension of 30 g, resulting in ≈ 400 kg of effective mass load on each endplate. In contrast, the effective gravitational load of each endplate, with its corresponding circuit boards, electronics, and cables, comprised about 60 kg. The pre-tension wires were released in stages and eventually removed during sector stringing. The stereo wires exerted the equivalent of about 14 kg of shearing force which tended to distort the chamber sectors. However, tests showed that the structure was rigid enough so that wire tensions were not significantly affected.

A second effect, peculiar only to the R1 wires, resulted from gravitational forces acting on the long, thin endplates. During construction, each sector was supported by its ends in an orientation such that the wires could be strung vertically. However, in this orientation the gravitational forces on the endplates, and hence the endplate distortions, were at a maximum. The temporary posts maintained the relative spacing between the endplates to high precision, but gravity acted to deflect the center of each endplate downward by 6 mm. Thus, the axial wires, which were exactly parallel to the posts, were unaffected by this effect, as both endplates had identical gravitational sags. However, due to the slight angle of the stereo wires, their length was slightly increased or decreased, depending upon which direction the sector was rotated from its "sag-free" endplate orientation, or the orientation with the wires running horizontally. This sagging of the endplates during sector stringing had to be taken into account in order to allow all wire tensions to fall within tolerance when the six sectors were integrated together. By correctly adjusting the stringing tensions along the length of the sector, and proper selection of the number of pre-tension release steps, the final wire tensions in the sag-free orientation were kept to within 20% of their nominal values.

2.6. Region-two construction

The R2 chambers, which were designed and constructed by Old Dominion University with assistance from Jefferson Laboratory, are in the middle of the three nested drift-chamber packages. They track all charged particles in the magnetic field of the torus near the point of maximum sagitta. The six identical R2 sectors are 4.4 m long, 40 cm wide radially, and span nearly 2 m at their widest point. They are located at a radius of ≈ 2 m from the nominal target location. The endplates are attached directly to the torus cryostats. At the location of the R2 chambers, the shadow region extends outward by ≈ 5 cm from the face of the torus cryostat. All chamber support hardware and electronics had to fit entirely within this space.

Each R2 sector contains a total of 2262 hexagonal drift cells ranging in diameter from 26 to 29 mm, with cell size increasing uniformly with wire layer number. The wires are arranged in two superlayers, one axial (at smaller radius) and one stereo

(at larger radius). Each superlayer contains six layers of between 184 and 192 drift cells. One of the two endplates in each chamber has a 2.54-cm step away from the cryostat to avoid a cryostat projection that decreases the azimuthal coverage slightly for $\theta \geq 120^{\circ}$. The hexagonal wire pattern is unaffected by this step.

Fig. 3 shows the positioning of the endplates with respect to the magnet cryostat. The length of the endplates was determined by the required CLAS polar angle coverage. The radial width of the endplates was determined by the space required for the two superlayers, pre-tension wires between the superlayers, gas window attachments, and structural supports. The endplate thickness was determined by requiring that the endplate deform less than 0.5 mm at its center under the full load of the wire tensions.

Several design constraints were peculiar to R2. These chambers have to operate in a magnetic field up to 2 T, and the chambers have to withstand any rapid changes in magnetic field, such as what might occur due to a magnet quench. The chambers also have to withstand movements of the cryostats by up to 2 mm. This can occur if the cryostat is brought up to ambient pressure.

The R2 endplates are constructed from 2-cm thick Stesalit 4411W, a disordered epoxy-fiberglass composite commonly used in wire–chamber construction [11,12], and known not to cause aging problems [13]. Using a nonconducting material eliminates any possible forces on the endplate due to eddy currents produced during a magnetic-field quench. It also allows the trumpets that position the wires to be essentially flush with the endplates, rather than having to insulate the trumpets from the conducting endplates as in the other two Regions (see Fig. 8). This reduced the thickness of the inactive region by 1–2 cm.

Not shown in Fig. 8 are the inner and outer gas windows made of 15-μm aluminized nylon. Gas was supplied to the downstream end of each sector through a 0.6-cm diameter gas line running longitudinally over the endplate. Gas was exhausted through a low-impedance 2.5-cm diameter manifold at the upstream end.

In order to support the load of the wire tensions and the weight of the chamber frame, the endplates had to be supported at various points along their periphery during both construction and installation. The load distorted the endplates over their radial width and along the length between supports on the order of 0.5 mm. Finite-element analysis of the endplates showed that, in addition to the sector and back-plates, each endplate required support at 25 points along its periphery to reduce the between-support endplate distortion to less than the distortion across their width.

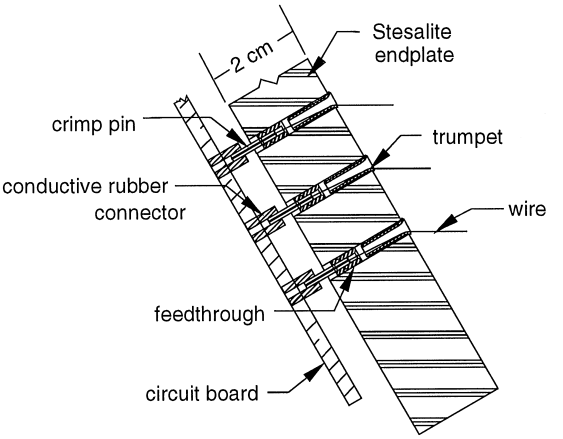

Fig. 8. Schematic cross-sectional view of the R2 endplate wire-positioning hardware.

In order to support the sectors during stringing and transport, and to control the endplate spacing, 25 temporary 2.54-cm diameter adjustable-length aluminum posts connected the two opposite endplates. The posts attached to the endplates with a ball-and-socket joint for ease of removal. Adjacent posts were diagonally connected to each other by a hollow 2.54-cm diameter aluminum tube in order to eliminate chamber distortion. Following insertion of the chambers into CLAS, each endplate was connected to the magnet cryostat at 25 points, and the posts were removed. The tension transfer from the posts to the permanent supports is discussed in more detail in Section 3.2.

To assemble the chamber hardware into a frame with better than 1 mm accuracy, a specialized assembly fixture was constructed. This assembly allowed each endplate to be positioned individually to a tolerance of 100 μm before the two endplates

were connected by the posts. The completed chamber frame was then attached to a steel "strongback" at four points. All subsequent manipulations of the chamber were done via the strongback in order to minimize stresses on the chamber.

The hardware used to hold and position the wires is shown in Fig. 8. The stainless-steel trumpets were glued into the endplate holes with the flare of the trumpet resting on the surface of the endplate. A polyolefin shrinkwrap sleeve placed around each trumpet helped to keep it centered and straight. Wire spacing on the 36-cell R2 prototype chamber varied by only ± 50 μm FWHM, thus demonstrating the precision of the technique [14]. A separate plastic feedthrough was glued into each hole to a precise depth. The inner diameter of the feedthrough was matched to the wire crimp pin. All wire-feedthrough hardware was installed in the endplates prior to frame assembly. The shrinkwrap sleeves were placed on the trumpets before the feedthroughs and trumpets were glued into the endplates.

To prevent endplate deformation during stringing, 88 pre-tension wires made of steel fishing leader were pre-strung in special holes between the two superlayers at a tension of 9.6 kg each, using large springs. The pre-tension wires were individually removed as the field and guard wires were strung at a tension of 140 g. The sense wires were strung last at a tension of 19 g. Due to the large ratio of wire tension to endplate weight, wire tensions were unaffected by chamber orientation. After each chamber was fully strung, all of the wire tensions were measured. Those with tensions more than 25% from nominal were removed and replaced. Wires were strung in some of the pre-tension holes for tension testing during and after sector installation.

2.7. Region-three construction

The R3 chambers were designed and constructed at Jefferson Laboratory. The shape of each 7-m long sector follows the outer contour of the CLAS torus. The sectors are located outside of the toroid in a field-free region at a distance from the target of between 3.0 and 3.5 m. Each chamber has 2304 hexagonal drift cells ranging in diameter from 40 to 45 mm, with cell size increasing uniformly with layer number. The wires are laid out with the axial superlayer closer to the target. Each of the 12 wire layers contains 192 drift cells.

The endplates are a composite assembly consisting of 1-mm thick, pre-drilled stainless-steel skins sandwiching 5-cm thick pre-drilled structural foam enclosed with aluminum close-out pieces about the perimeter of the foam. The two endplates of each chamber are held apart at their outer radius by a curving 3-cm thick composite shell made from 300-μm skins of carbon fiber, sandwiching a Nomex-paper honeycomb. Fig. 9 shows a cross section of the skin-to-endplate junction. Along the inner radius are five equally spaced, thin-walled carbon-fiber cylinders keeping the endplates apart. Choices for these materials were driven by multiple-scattering considerations and the desire to combine strength with light weight. Because the R3 chambers are located farthest from the target where more space is available, it was possible to include extra material to build a very rigid, self-supporting structure, thus avoiding some of the special challenges for tension transfer peculiar to R1 and R2.

The endplate hole-position accuracy for the wire feedthrough penetrations was maintained to

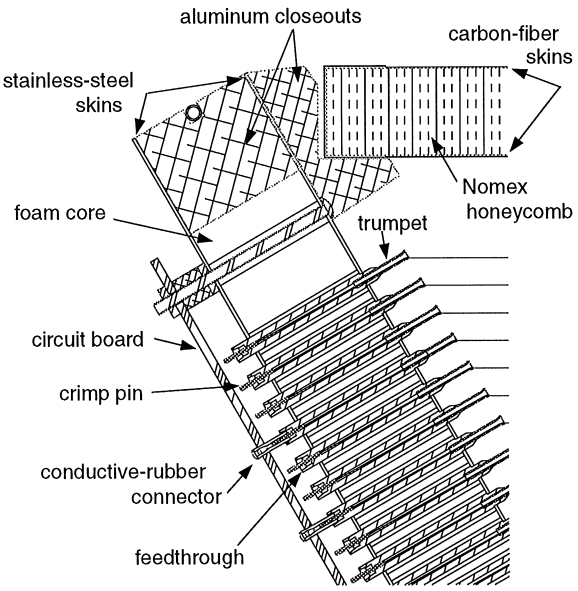

Fig. 9. Schematic cross-sectional view of an R3 endplate highlighting the wire-positioning and chamber-frame hardware.

50 μm. Before stringing began, the feedthrough assemblies were glued into the endplates and the sectors were pre-tensioned. This was accomplished with large springs to simulate the load of the tensioned wires. The goal during stringing was to keep all wires to within $\pm$ 10% of nominal tension. The few percent of wires that were outside of this tolerance were replaced. The guard wires served the dual function of shaping the electric field around the perimeter of the superlayers and pre-stressing the endplates prior to stringing. The sense wires were tensioned at 18 g and field and guard wires were tensioned at 134 g. Their relative values were chosen to ensure matching local gravitational sag for all the wires [15].

A 1-cm diameter gas input line running longitudinally over the endplates distributed the gas to the downstream end of the chamber. Gas was exhausted through a low-impedance 2.5-cm diameter manifold at the upstream end. The gas window on the inner radius was made from 15-μm aluminized nylon. All of the chamber utilities remained within the shadow of the torus cryostats or beyond the 142° angle of acceptance.

3. Installation and alignment

3.1. Region-one integration and installation

The sequence of operations during the R1 integration and installation is illustrated in Fig. 10. The integration of the six R1 sectors into a single unit was performed with the symmetry axis of the detector oriented vertically. Tests with the prototype showed that lifting the sectors into this orientation did not overstress any of the wires. The struts that held the temporary posts in place also functioned as the joining brackets between sectors (see Fig. 7). The final step in the integration process was the tension transfer procedure, in which the load due to the wires was transferred from compression in the posts to balanced tension among the sector endplates. This iterative process ultimately allowed the posts to be removed entirely without affecting any of the wire tensions. This was accomplished by inserting shims accurate to 50 μm between struts from neighboring endplates to maintain their spacing before bolting them together. Once the struts were locked together the posts were removed.

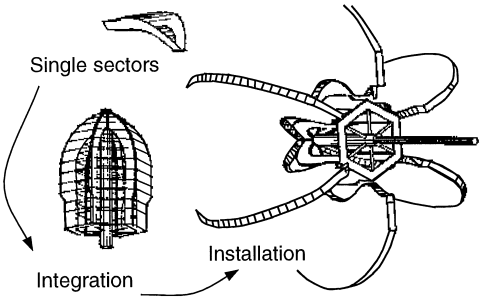

Fig. 10. Sequence of operations from R1 sector assembly through detector integration and installation into the CLAS torus. Following the final step, the temporary steel-pipe assembly was removed.

Stresses were placed on the sectors as they were connected to each other on the support ring. To monitor the stresses, wire tensions were measured at 30 locations around each sector [16]. Throughout the assembly, measurements were repeatedly made to ensure that tensions remained within acceptable limits. The goal during the tension-transfer procedure was to keep the tensions on the wires to within $\pm$ 10% of their strung values.

Once the detector was fully integrated and loaded down with cables, the wire tensions were measured as the detector was rotated from its vertical assembly position to the horizontal position it would assume within CLAS. The detector has a weight of $\approx$ 800 kg, about 20% of which is cable weight. It was found that the wire tensions remained within the $\pm$ 10% allowed tolerances throughout the test.

After transport in a vertical orientation to the experimental area, the detector was rotated into its horizontal position and supported on a steel pipe. This pipe was cantilevered from a rail-mounted installation cart that provided the ability to rotate the chamber about its axis, as well as to translate it horizontally and vertically. These degrees of freedom were required to insert the chamber through the narrow upstream opening of the torus cryostat, to engage the docking dowel pins on the downstream end of the detector, and to attach the support legs on the upstream end. When the mechanical load of R1 was securely supported by the

cryostat, the pipe assembly and cart were disengaged from the detector. Finally, all signal, electrical, and gas connections to the sectors were made.

3.2. Region-two installation

Each R2 chamber was inserted into the torus on a system of rails that guided it from a cart, located downstream of the torus, into position between the cryostats. Once inserted into the torus, the location of each R2 chamber parallel to the plane of its upper-adjacent cryostat was fixed by dowel pins inserted into two "pin blocks" fastened to the cryostat on the "fixed-endplate" side of the sector. The location of the chamber in the direction perpendicular to that cryostat was fixed by 25 "attachment blocks". The position of the pin blocks and the heights of the attachment blocks relative to the cryostat were transferred from a precision template that was surveyed into position with an accuracy of 100 μm prior to chamber insertion. The chamber was bolted to the attachment blocks through holes in the endplate, after which it conformed to a plane, thus removing any distortions of the chamber shape due to its weight.

The other endplate, referred to as the "spring-side" endplate, was not fastened rigidly to its cryostat, but held in place by a pair of double hinges, which only allow motion perpendicular to the cryostat, and 25 adjustable springs attached to the cryostat through holes in the endplates. This system was used to transfer the wire tensions from the temporary posts to the cryostat. This allows for motions up to 2 mm of the cryostat surface perpendicular to its plane without changing the wire tensions by more than $\pm$ 20%.

The tension-transfer process utilized the length adjustability of the posts. One end of each 2.54-cm diameter aluminum post included a 7.5-cm deep, 1.4-cm diameter hole. During chamber fabrication a matching diameter "screw adjuster" was inserted into this hole and then attached to the endplate as shown in Fig. 11. The depth of the screw adjuster within the hole was self-adjusting so that the attachment to the endplate was made without stress. The screw adjuster was then held in place within the hole by a clamp around the post. The screw adjuster also has a pair of nuts and a washer to act as a stop, preventing the screw adjuster from moving into the post. Once the chamber was in place and the strongback was removed, a gap of 250 μm was set between the end of the post and the washer/nuts on the screw adjuster. The clamp was then released, causing the screw adjuster to move into the post until the nuts came into contact with the post. This step acted to relax the wire tensions somewhat. After this was done for all 25 post assemblies, the springs were fastened to the cryostat. The tensions in the springs were adjusted iteratively until the 250-μm gap for each post assembly was recovered to within 50 μm. This procedure generally resulted in wire tension restoration of $\pm$ 50% of the pre-installation tension. The springs were then further adjusted while the tension in specially instrumented wires was monitored. With a few exceptions, the pre-installation wire tensions were recovered to within 20%.

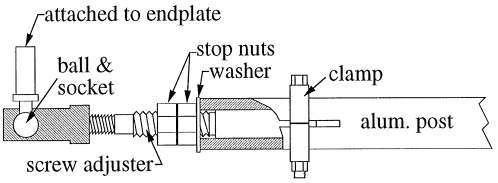

Fig. 11. Spring-side end of an R2 adjustable post assembly partially cut away to show the screw adjuster on the inside of post.

After completion of the tension transfer process, the insertion rails were removed from the torus. Finally, the signal, electrical, and gas connections were made. Dry-air lines were also connected so that the temperature and humidity of the on-chamber electronics could be controlled. One R2 sector is shown in its installed position in Fig. 12.

3.3. Region-three installation

The R3 chambers are attached to the outside edges of the cryostats. Each chamber is attached at three points across two cryostats as shown in Fig. 12. The positions of these points were predetermined and set using a computerized multi-headed theodolite system that accurately measured locations in space. The gravitational sag of the attachment fixtures was also taken into account.

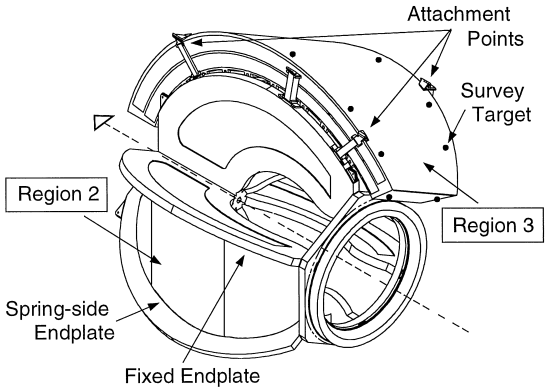

Fig. 12. An R2 chamber (lower left) and an R3 chamber (upper right) shown in their installed positions on the torus cryostat. For the R2 chamber the locations of the fixed and the spring-side endplates are labeled. For the R3 chamber the three attachment points and survey targets are labeled.

Each R3 chamber was transported to the experimental area attached to its own steel strongback, similar in design to those used for R2. These strongbacks were attached to temporary rail assemblies installed around the outside of the cryostat. The chambers were then moved along these rails until the three attachment points were aligned. After ensuring that the chamber was electrically isolated from the cryostat, the chamber was bolted into position. Due to the much more rigid nature of the R3 chambers, no tension-transfer procedures were necessary. Mechanical tests in the clean room indicated that the wire tensions were unaffected during the series of rotations and movements of the sectors used during installation. After the chamber was bolted into position, the strongback was removed and the rail system was then reconfigured for the next sector. Finally, all chamber signal, electrical, and gas connections were made.

3.4. Chamber survey

Unlike the R1 chambers, which were surveyed as a single system subsequent to installation [17], each of the R2 and R3 sectors was surveyed individually after installation. For R2, the position of the installation fixtures was surveyed in order to determine the position of the fixed-endplate side of the chamber. In addition, the inner radius of each endplate was surveyed after sector installation. The R2 survey was fully completed before R1 and R3 installation began, as they obscured all R2 sighting fiducials. The R3 chambers were surveyed by sighting the locations of multiple targets positioned along the carbon-fiber skins relative to fixed reference monuments in the experimental area to determine their absolute position in space. The locations of the chamber targets for R3 are illustrated in Fig. 12. The accuracy of the measured positions of all chambers was determined through detailed tracking studies (see Section 7.2).

4. Chamber electronics

4.1. Overview

The signal connections to the wires are made through printed-circuit boards mounted along one side of each chamber. These boards are responsible for signal routing and pre-amplification. On the opposite side of each sector, another set of circuit boards is responsible to make the high-voltage connections to the wires. Fig. 13 provides a schematic representation of the overall electronics layout from the chamber circuit board at one end to the timing electronics at the other.

4.2. On-chamber electronics

4.2.1. Signal translation boards

The signal side of each chamber is tiled with multi-layer printed circuit boards called Signal Translation Boards (STBs). These boards were designed to capacitively decouple high voltage from the signals, and then to route the signals to the single in-line package (SIP) transimpedance preamplifiers mounted on these boards. The amplified differential signals are then sent via 20-m long twisted-pair lines to the main CLAS readout electronics.

The connections between the sense-wire crimp pins and the plated-through holes of the STB boards are made using short conductive-rubber tubes. This material consists of silver-plated and/or nickel-plated glass spheres embedded in a silicon-rubber matrix. These tubes pass through the

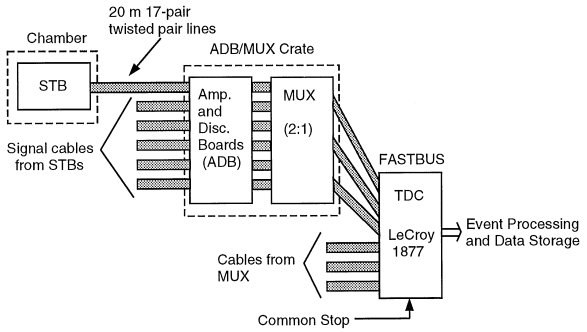

Fig. 13. Schematic representation of the overall electronics layout for chamber readout. At the chamber, a circuit board is responsible for signal routing and pre-amplification. The signals are then sent to boards which amplify and discriminate the signals before the input the timing electronics.

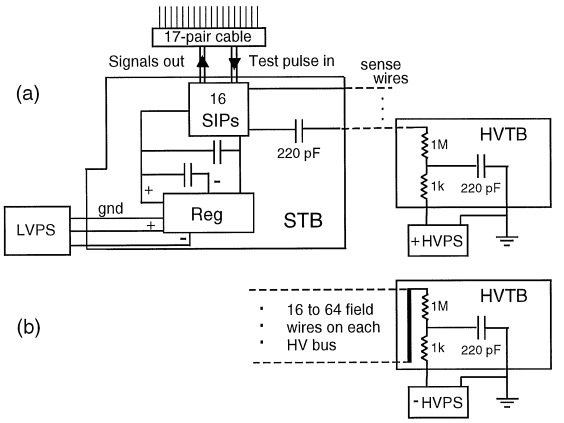

Fig. 14. Schematic representation of the STB and HVTB configurations for (a) the sense wires and (b) the field wires, showing the low- and high-voltage power supplies (PS). The test pulse on each STB cable, described in the text, feeds the 16 SIPs that are read out through a single STB cable.

plated-through hole and over the end of the crimp pins, making the electrical contract between the wire and the circuit board. A small plastic cap inserted into the end of the tube ensures good contact with the circuit board. This approach has the advantages of reducing the space needed for connections, preventing crimp pins from being pulled from the feedthroughs when disconnecting the boards from the wires, and reducing the cost compared to metal connectors.

The basic signal-side circuit for the sense wires is shown in Fig. 14a. The STB boards include the low-voltage connections to power the pre-amplifiers, and the regulators necessary to ensure that a steady, clean DC voltage is supplied. The signal-cable connectors are positioned at the outer edge of each STB. Each R1 chamber has 10 STB boards with 64 to 160 SIPs per board, each R2 chamber has 13 STBs with 192 SIPs per board, and each R3 chamber has 48 STBs with 48 SIPs per board.

The SIP pre-amplifiers were designed specifically for CLAS [18]. These amplifiers have complementary outputs designed to amplify signals by a factor of 2.25 mV/μA. Besides high gain, characteristics of the SIPs include: fast rise and fall time (3–4 ns), wide frequency bandwidth, wide dynamic range, and low noise and power dissipation (65 mW). The power requirement for a single SIP is 5 VDC at 13 mA, and is supplied by the low-voltage system described in Section 4.4.2.

4.2.2. High-voltage translation boards

The high-voltage side of each chamber is tiled with single-layer printed circuit boards known as High-Voltage Translation Boards (HVTBs). Connections between the chambers and the sense, field, and guard high-voltage cables are made through solder terminations on the HVTBs. The 10–20-m long high-voltage cables were soldered to a distribution board on the endplates on one end and terminated into a custom high-voltage connector on the other. Enough slack was left in the cables to allow withdrawal of the chambers for service work.

Horizontal rows of field-wire crimp pins are wire wrapped together with gold-plated copper wire in small groups. The guard wires surrounding the perimeter of each superlayer are also wire wrapped together. Both the field and guard-wire busses are capacitively coupled to ground. The sense wires are daisy chained in small groups on the HVTBs.

Each R1 chamber has 6 HVTBs, each R2 chamber has 25 HVTBs, and each R3 chamber has 48 HVTBs. The R2 and R3 HVTBs have essentially equal numbers of wires on each board. The segmentation of the chambers into multiple high-voltage input lines was included to minimize the number of drift cells lost in case of any broken wires. At nominal design luminosity the chamber currents in the outer two regions were not expected

to necessitate any further segmentation. However, in the case of the R1 chambers, as they are closest to the target and see the highest flux of charged particles, careful layout of the HVTBs was essential to roughly equalize the currents on the high-voltage supply channels. The HVTBs at smaller angles (downstream end of sector) supply voltage to fewer wires than those at larger angles (upstream end of sector). The number of wires per high-voltage channel ranges from 16 to 64.

The high-voltage configurations for the sense and field wires are shown in Fig. 14. Connections to the field and guard wires are made via 22-AWG wires running from the HVTB to the individual busses. Connections to the sense wires are made via the same conductive-rubber tubes used on the signal side of the chambers.

4.3. Off-chamber electronics

4.3.1. Amplifier/discriminator boards

The amplified chamber signals are read out through custom-built front-end electronics crates. Each of these 31 crates contains 12 Amplifier/Discriminator Boards (ADBs), 12 back-plane mounted multiplexer (MUX) boards, and modular power supplies. These VXI-sized crates also provide adequate cooling for the installed electronics.

Each ADB has 96 channels that amplify and discriminate the pulses fed from the SIPs through the 20-m long twisted pair cables. For each ADB connector, there are 16 pairs of complementary signal inputs and one pulse output for remote pulsing of the SIPs (see Section 7.3).

The amplifier section consists of a bipolar pseudo-difference amplifier set for a nominal gain of 30. The limiting-feedback network decreases the overall gain when the input-to-output amplitude difference exceeds the Schottky diode forward conduction characteristic of 350 mV, thus extending the dynamic range and reducing saturation conditions at high gain. A nominal gain of 30 is obtained for input signal amplitudes below 10 mV, and the effective gain is decreased to a factor of 11 once the input signal amplitude exceeds 10 mV. This transition corresponds to a chamber current signal of about 9 μA for a pre-amplifier gain of 2.25 mV/μA and a 50% signal loss through the cable.

The amplified signals are then fed to the discriminator section that consists of a comparator, pulse-width adjustment circuitry, and an output level translator. A front-panel potentiometer is used to set the threshold level for all 96 channels on a board. Thresholds of approximately 35 mV at the comparators correspond to roughly 1 μA drift-chamber signals. The thresholds were set to -30 mV for R1 and R2, and -45 mV for R3; see Section 6.1.1.

The pulse-width adjustment circuitry is used to set the output width of the channels into two groups of 48 channels each. In this manner, two channels with different pulse widths can be multiplexed together. The identity of the fired channel is recovered from the pulse-width information. Two ADB versions were manufactured with different pulse-width ranges to account for the different drift-time ranges of the chambers. R1 employs an ADB version with 350 and 450 ns output widths; R2 and R3 employ an ADB version with 1000 and 1200 ns output widths.

Each ADB is also provided with circuitry for calibration in groups of 16 channels. Analog calibration signals are input through the front panel, and group selection is decoded from back-plane signals supplied from Trigger Calibration Interface boards. There is one such board for each ADB crate.

4.3.2. Multiplexer boards

To reduce the cost for the readout electronics, the discriminated pulses from pairs of wires are multiplexed into one timing channel in custom-built boards. This multiplexing preserves the information from each signal via an exclusive OR (XOR). Depending on whether one or both multiplexed wires fire in a given event, there can be 2, 3, or 4 pulse edges, or voltage transitions, presented to the time-to-digital converters (TDCs) for digitization. If only one signal is present, the TDC records 2 pulse edges, corresponding to the leading and trailing edges of the discriminator output pulse, with the leading-edge time assigned as the drift time. If two multiplexed wires fire in a given event, then 3 or 4 pulse edges can be digitized. Pulse edges closer together than ≈ 5 ns cannot be resolved by the TDC. As the multiplexed signal pairs have

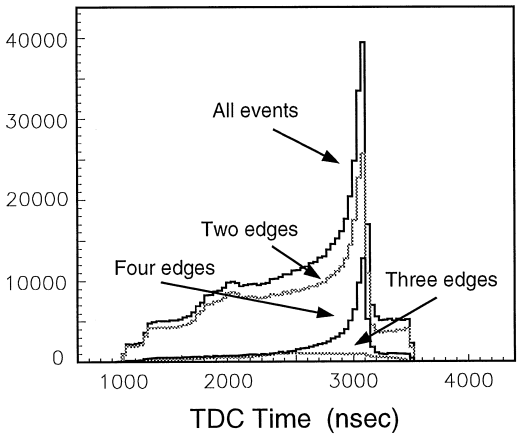

Fig. 15. TDC histogram for one R3 sector showing the contribution of two, three, and four pulse-edge events.

different output pulse widths, distinct combinations of pulse edges in the XOR signal can then be examined to determine the appropriate times to assign to the hits.

A software algorithm is applied to the multiplexed signals to retrieve the wire time and identification. Fig. 15 shows the contribution of 2, 3, and 4 pulse-edge events to a TDC time spectrum. Two-edge events account for most of the data. This is expected since multiplexed wires are separated by four drift cells in order to reduce the probability that both wires fire in any given event. The three-edge events include a number of different contributions. They include two valid wire hits, i.e. both members of the multiplexed pair, in which two of the four edges occur too close together in time to be resolved by the TDC, and four-edge events where one pulse edge falls outside of the TDC time window and is not digitized. In principle, both of these event types can be reconstructed by the analysis software. Coherent noise causes multiplexed channels to have their leading edges in time. Only one leading edge is digitized because of the finite double-pulse resolution of the TDC. This three-edge event class washes out the timing structure of the valid events in the raw TDC spectrum.

4.3.3. Timing electronics

The LeCroy 1877 TDCs used for chamber readout are 96-input FASTBUS-standard boards. Each input records the time of a logic voltage signal with a least-significant bit resolution of 0.5 ns within an adjustable-time window of duration up to 32 μs for up to 16 pulse edges. Chamber readout requires 186 of these boards.

These units were thoroughly studied on the bench before installation. The primary test was to study the integral linearity of each board. Problems with this aspect of the TDCs would affect the timing calibrations in the tracking routines, leading to an increased error in the momentum measurement. The tests for integral linearity studied the TDC response over its full 32 μs range with input timing pulses. These data were fit to a straight line, and then compared with the expected slope of 0.5 ns per channel. TDCs were rejected if the fitted peak centroid at any calibration point in the full time range deviated from the expected value by more than 1 ns. In addition, the differential non-linearity and several function checks such as double-pulse resolution were tested on each TDC board.

4.4. Power systems

4.4.1. High-voltage system

The chamber high voltage is supplied by three CAEN 527 high-voltage mainframes, each containing 10 boards with 24 channels per board. The high-voltage channels are further multiplexed through a distribution box before being delivered to the chambers. Each high-voltage channel supplies either a negative or a positive voltage at a maximum current of 40 μA.

Real-time control software was designed for the CAEN power supplies to provide a fast-control environment to manage all high-voltage hardware operations. A high-level graphical user interface was designed to control and visualize all monitoring results. The program allows control over such parameters as voltage settings, ramp rates, and maximum current and voltage settings.

The high-voltage cables consist of 12 Teflon-insulated 22-AWG stranded conductors shielded with a copper braid. The copper-braid shielding over the conductors was required to have 90% or more coverage to prevent voltage fluctuations due to induced noise. The entire 12-conductor assembly was encapsulated in an outer PVC jacket. The

average high-voltage cable length from the chambers to the high-voltage distribution boxes is about 20 m. The voltage drop across this length is negligible.

4.4.2. Low-voltage system

Each chamber has its own dedicated supply to provide power to the SIPs. The low-voltage distribution system was designed to provide a minimum of 6 V at the STBs so that the voltage regulators could maintain a constant 5-V potential for the SIPs. The power supplies chosen were Hewlett Packard 6651A units that have a maximum output of 8 V at 50 A. These supplies have over-current, over-voltage, and thermal protection. Trip levels for the over-current and over-voltage conditions were adjustable to at least 120% of the nominal output levels. If a trip condition is detected for current, voltage, or temperature, the power supplies automatically shut down and remain off until a reset has taken place. For safety purposes, an in-line fuse is included for each low-voltage conductor. Control software reads the current and voltage from each of the 18 low-voltage supplies. The system provides an alarm if a trip condition has been sensed and provides for remote reset of the individual supplies.

The low-voltage power cables each consist of a pair of conductors shielded with copper braid and insulated in a PVC jacket. To minimize the voltage drop, each conductor is 16-AWG stranded copper wire. The maximum allowable voltage drop along the entire 20-m long cable was 2 V.

5. Gas system

High-purity gas mixtures are delivered to the chambers by means of a gas-handling system designed and built by a collaboration of Jefferson Laboratory and the University of Richmond. Two systems exist for mixing gas; one services R1 and R3, and the other services R2. This allows R2, which is located with a high magnetic field, to be supplied with a gas mixture having the higher drift speeds that are favored in such environments. As stated in Section 1, all three Regions are now using the same 90% argon–10% CO_2 gas mixture. Each region has its own supply and return circuits. During normal operation, typical flow rates per sector are 0.2 l/min for R1, 3.3 l/min for R2, and 4 l/min for R3. A schematic diagram of the basic circuit for each Region is shown in Fig. 16.

During steady-state operation, fresh gases are precisely mixed using mass-flow controllers (MFCs) to achieve the correct gas-mixture ratio. This ratio is set and continuously monitored using Panametrics thermal-conductivity units. The mixed gas is stored in large buffer tanks supplying the process loops that contain the chambers. These tanks contain enough gas for several days of operation in the event of a problem with the bulk supply or the mixing equipment. As the mixed gas enters the supply loops, the pressure is reduced, the gas is filtered to remove contaminants, and the oxygen and moisture contents are measured.

The filter system for the gas consists of two BOC gas filters. The first is a molecular sieve (4A-Z8 and 13X-78) to remove water, oil, and organics from the gas. The second is a sintered bronze type with 5 μm elements to remove particulate contamination before it could reach the MFCs. The oxygen content of the gas is monitored with a Teledyne model 300 T trace oxygen analysis system, and the water content is monitored with Panametrics Moisture

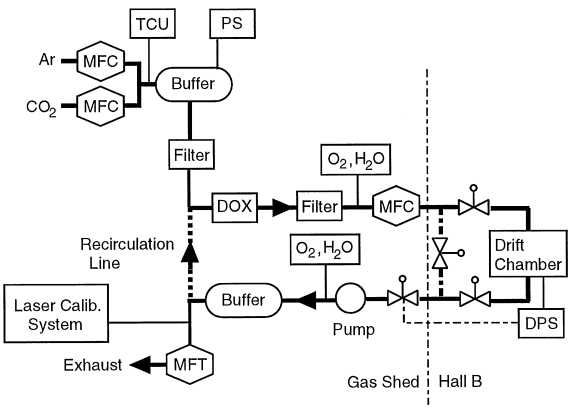

Fig. 16. Schematic diagram of the gas-distribution system for each Region, showing the location of mass-flow controllers (MFC), thermal-conductivity units (TCU), pressure sensors (PS), filters, De-Oxo catalyzres (DOX), oxygen and water sensors (O_2, H_2O), the mass-flow transducer (MFT), and the differential-pressure sensors (DPS).

Image series probes and readouts. After the filter system, the gas then flows from the gas shed to the hall.

The flow rate is controlled by MFCs for R2 and R3, and by a vernier-scaled throttle valve for R1. In the hall, the gas enters the supply manifolds and then flows through the six sectors of each region in parallel. The gas exits the individual sectors and enters the exhaust manifolds where the differential pressures with respect to atmosphere are monitored. These pressure readings are transmitted back to the gas shed where they are used to control proportioning solenoid valves in front of the pumps. The pumps pull gas out of the chambers while controlling the pressures in the chambers. In case of equipment failure, power loss, or extraordinary over- or under-pressure transients, the chambers are protected by safety bubblers.

Gas exhausted from the return pumps is vented to the atmosphere, or can flow out to the buffer tanks for reuse during recirculation operation. During recirculation operation, which as of 1999 is not yet implemented, a fraction of the gas will be exhausted and the rest will pass through De-Oxo catalyzers and molecular sieves to remove oxygen and water contamination, and will then be monitored by O_2 and H_2O sensors before being returned to the chambers.

The various sensors are powered and monitored with low-level hardware controllers that have local readout and programming capabilities. Some of these instruments are programmed to produce signals that are used to control or bypass parts of the system. The flow controllers and transducers are operated with two MKS 647A MFCs. Three MKS 146B vacuum-gauge measurement and control systems are used to monitor the pressures in the chambers and to control the proportioning solenoid valves in front of the pumps. An Omega DP25-E process meter is used to monitor the differential pressure at the chamber exhaust manifold and control solenoid valves that isolate the chambers from the gas system in the event of a system failure or power loss. These safety features are hardwired and under no software control. A computer control system is used to monitor analog outputs from the instruments and to archive parameters for analysis [19].

6. Commissioning

6.1. Setting operational parameters

The chamber-operating parameters include the high-voltage potentials on the sense, field, and guard wires, the discriminator thresholds applied before time digitization, and the adjustable-time delays and windows used in digitization of the time signals. The basic requirements are that the chambers operate with high efficiency, low accidental occupancy, and at a minimal gain to maximize chamber lifetime.

6.1.1. Discriminator thresholds

The ADB discriminator thresholds must be high enough to reject electronics noise; however, the lower they can be set, the lower the required gas gain can be for efficient chamber operation. The electronic noise levels in a typical R2 chamber at the input to the ADB, shown in Fig. 17, peak near 90°, the region of the detector with the longest wires. The noise levels in all chambers have been found to be stable with time.

The ADB thresholds, -30 mV for R1 and R2, and -45 mV for R3, were chosen from studies of the chamber drift-cell hit occupancy as a function

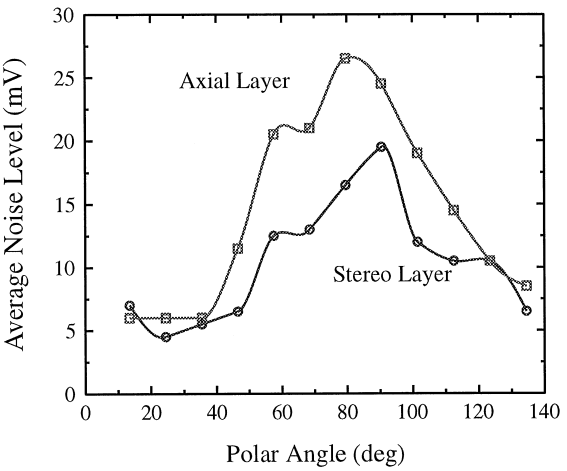

Fig. 17. Measured average noise levels in a typical R2 chamber at the input to the ADB (terminated into 50 Ω) as a function of the polar angle for both superlayers. The curves serve only to guide the eye.

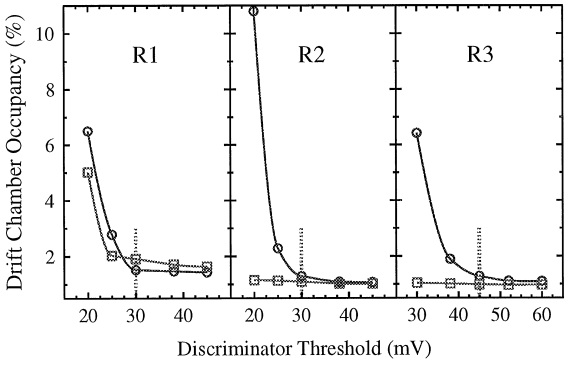

Fig. 18. Chamber hit occupancy as a function of ADB threshold. The square points correspond to the sector Region with the smallest number of noise-related hits, and the circles correspond to the sector in each Region with the largest number of noise-related hits. The vertical dashed lines mark the ADB threshold employed.

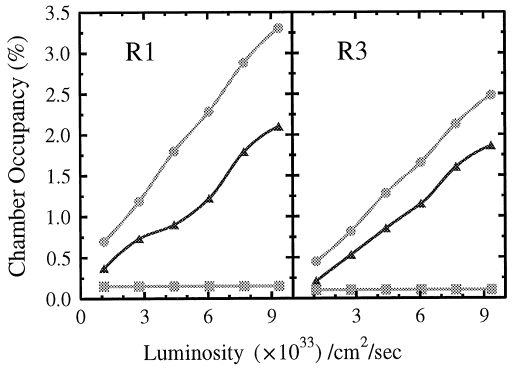

Fig. 19. Average drift-cell hit occupancy in R1 and R3 for all six sectors as a function of luminosity. The circles correspond to the occupancy including all chamber hits, triangles represent hits unrelated to tracks, and squares represent the cosmic-ray contribution.

of the ADB threshold as shown in Fig. 18, acquired at a luminosity of $\approx 4\times10^{33}$ cm^{-2} s^{-1}. The data in each Region revealed that above a particular threshold the chamber occupancy flattened out. The operating thresholds were set to be just above this point, keeping the electronic-noise contribution to the hit-wire occupancy to below 2%.

The chamber hit occupancies are shown as a function of luminosity in Fig. 19 at nominal operating voltages for both R1 (the chamber closest to the target) and R3 (the chamber farthest from the target). From this figure it is clear that the average accidental occupancies are well below 5% at full design luminosity. Note that this occupancy is strongly affected by the mini-torus shielding magnet which prevents Møller electrons from entering the chambers; see Section 8.1 for further details.

6.1.2. High-voltage plateau

Once the discriminator thresholds were set, a high-voltage plateau study was conducted in which the tracking efficiency was measured as a function of the voltage difference between the sense and field wires. The goal in setting the detector high voltages was to ensure that the tracking efficiencies were nearly 100% over the full extent of the drift cells for heavily ionizing particles such as protons, as well as for minimum ionizing particles such as pions.

Studies of prototype chambers and GARFIELD calculations [20] for the hexagonal cell geometry dictated that the best operating point for the drift cells is a setting where the field, sense, and guard voltages are roughly related as $-2V_f = V_s = 3V_g$. This configuration has been shown to minimize induced charge effects [2]. The guard voltages employed ensure that the drift cells along the perimeter of each superlayer have an electric field configuration nearly identical to that of the inner drift cells.

The chamber calibration relies on being sensitive to the first arriving electrons at the sense wire. Because the electronics amplification was the same for all chambers, all chambers were operated at the same gas gain. This gain was chosen to be $\approx 5\times10^4$ based on measurements with prototype CLAS chambers [21].[3] The corresponding operating voltages are given in Table 1. These vary from Region to fegion due to the different average cell sizes and ADB thresholds. In Fig. 20, the plateau curves are shown for the final ADB thresholds.

6.1.3. TDC setup

The chamber TDCs operate in common-stop mode. The start signal is provided from the

[3] The measured gain corresponds to that within a 200 ns time window.

Table 1
Drift chamber operating voltages

	V_s (V)	V_f (V)	V_g (V)
R1	+ 1266	− 633	+ 450
R2	+ 1400	− 700	+ 500
R3	+ 1500	− 750	+ 525

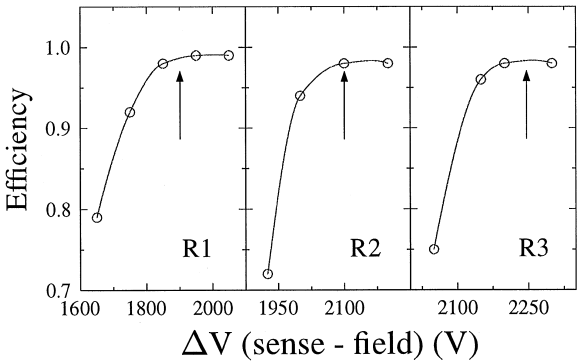

Fig. 20. Chamber efficiencies measured as a function of the voltage difference between the sense and field wires. The analysis selected negatively charged particles with momenta greater than 1 GeV/c. The arrows mark the nominal voltage settings.

individual wire hits, and the stop is provided by a delayed version of the CLAS trigger signal. The TDC readout requires optimization of two parameters for proper operation under all conditions. The first is the TDC time window which specifies how far back in time the TDC will record input starts relative to the stop. The second parameter is a delay for the input signals within the time window. The delay is applied uniformly to all TDC channels of a given Region by adding a programmable delay to the common stop signal fed into the FASTBUS crates. These delays were chosen to reasonably center the time distributions within the TDC time window.

The extent of the TDC time window was determined from considerations of the maximum possible drift time for each Region, and variations in this time due to changes in atmospheric conditions. Further considerations included CLAS trigger timing differences and TDC stop cable length differences to the electronics.

6.2. Data monitoring

6.2.1. Hit monitoring

A useful tool for monitoring the performance of the chambers during beam conditions is a two-dimensional occupancy plot of wire-layer number versus wire number for each sector. A representative histogram for one R2 chamber is shown in Fig. 21. Missing drift cells appear as holes in the distribution. With typical data rates of > 1 kHz, sufficient statistics can be acquired quickly to reveal any malfunction of the chamber system.

Another useful plot is that of the hit multiplicity for each of the chambers. Typical distributions for R1 and R2 are shown in Fig. 22. The R3

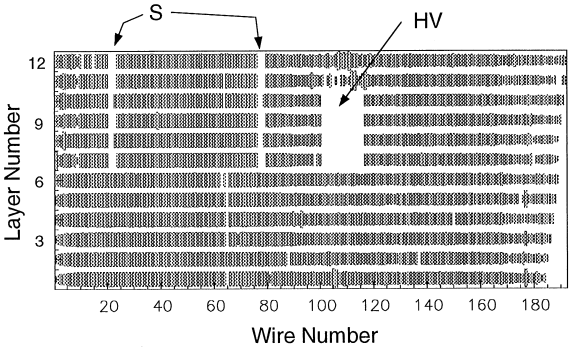

Fig. 21. Occupancy plot for one R2 chamber showing wire layer versus wire number. Two signal cable disconnections are present in this histogram (labeled by 'S') and one HV disconnection (labelled by 'HV'). Each different malfunction has a distinctive pattern in these histograms.

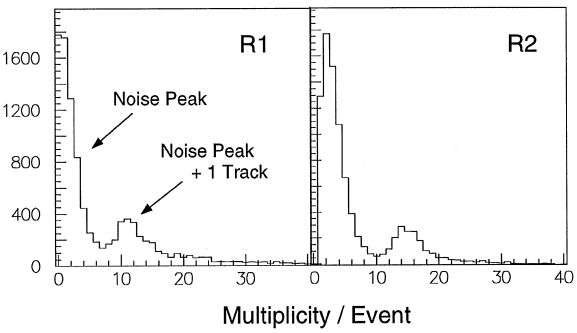

Fig. 22. Chamber hit multiplicity per event shown for typical R1 and R2 chambers with a low-current electron beam on a hydrogen target.

distribution is essentially identical to that of R2. These distributions are characteristically double-peaked. The peak at lower multiplicity corresponds to the background hits in the chamber, i.e. when there was no charged-particle track present. The peak at higher multiplicity corresponds to events including one charged-particle track coming from the target. Therefore, these events include the background plus either 10 or 12 additional hits due to the tracks passing through R1 or R2/R3, respectively. Tracking studies with higher-mass targets reveal smaller structures at still higher multiplicity corresponding to events with two or more charged-particle tracks in a given sector.

The performance of the drift-chamber system in conjunction with the rest of the CLAS detectors is monitored by performing full tracking reconstruction on a small fraction of the events on-line. This enables monitoring of data quality by extracting quantities like the number of hits per charged-particle track, the number of tracks per event, or the position and width of the elastic electron–proton scattering peak in the energy spectrum. The drift-chamber calibration and performance can be monitored by measuring the maximum drift time, residual distributions, and the occupancy plots for hits associated with tracks.

6.2.2. Time-spectrum monitoring

Monitoring the TDC time distributions provides confirmation that the gas drift velocity is roughly constant, and, therefore, that the gas purity and mixing ratio are acceptable, and information about noise. In Fig. 23 the TDC spectra for all hits within one chamber of each region are shown. The distributions of times for charged particles originating in the target sit on top of a flat background due to noise or accidental hits. The small step in these distributions at smaller TDC channel numbers is a feature that arises as one of the multiplexed signals has a longer input pulse into the TDC. This results in an effective difference in the time window for the two signals. Because the TDCs operate in common-stop mode, hits close to the sense wires give larger TDC times. This raw distribution is monitored for two characteristics, the width of the drift-time distribution on top of the background, and the size of this distribution relative to the noise pedestal. A change in the first could indicate a problem with the gas, while the second is a measure of the noise in the chambers.

In Fig. 23, the width of the drift-time distribution provides a measure of t_{max}, the maximum drift time for each region under standard conditions. This value can fluctuate by up to 20% due to changes in

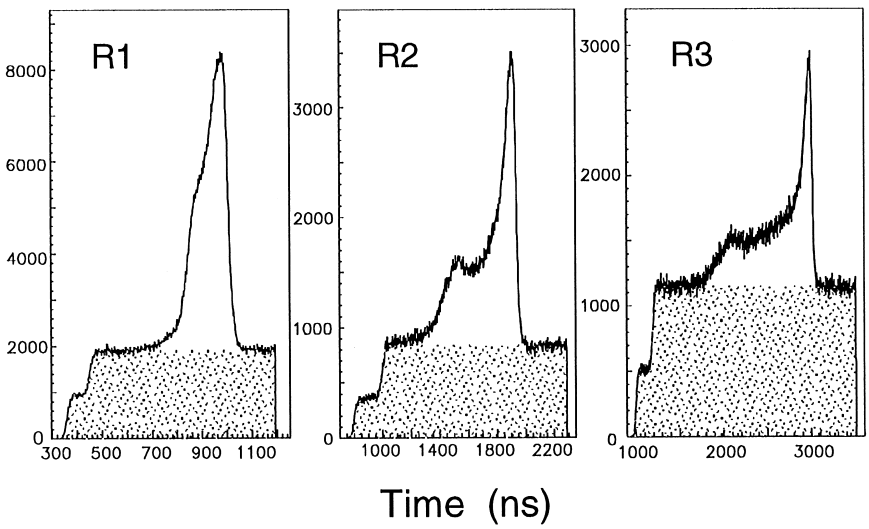

Fig. 23. Raw time spectra for all hits within one chamber of each Region. The shaded area of each spectrum represents the contribution from electronic noise.

atmospheric pressure and gas moisture content [22]. Typical values for t_{max} are 200 ns for R1, 500 ns for R2, and 1200 ns for R3. These spectra are for the raw TDC times not corrected for flight times or signal-propagation times.

6.2.3. Types of noise

A number of characteristic types of noise endemic to the system were identified during commissioning. Once the source of the noise was identified, it was possible to eliminate it in most cases. These sources of noise contributed to an elevated level of background hits in the detector. Most could be attributed to either electronic noise induced from ground current loops, or radiation backgrounds originating in the vicinity of the target.

Ground current loops were reduced by ensuring that there was no electrical contact between the chamber frames and the torus cryostat. Care was also taken to eliminate electrical contact between the signal-cable ground sheaths and the electronics ground. The background originating in the vicinity of the target appeared as a random scattering of hits uniformly distributed throughout the chamber volume. These arose mostly due to X-rays emitted when Møller electrons struck metal parts of the target assembly.

Time-difference distributions are useful to look for coherent noise, evident as spikes at fixed-time differences between pairs of drift cells. In Fig. 24 the distribution of time differences between all pairs of hits from one contiguous group of 96 wires is shown summed over all such groupings within two R2 chambers with different noise levels. Fig. 24a shows the expected mirroring of the normal time distribution about zero time difference with a small peak of coherent noise about zero. Fig. 24b shows a noise spike about zero as well as at several other times.

7. Calibration procedures

7.1. Track reconstruction overview

The reconstruction of charged-particle tracks is performed in two stages. In the first stage, individual tracks are fit only to hit-wire positions in a procedure known as "hit-based" tracking. In hit-based tracking, data are combined into track segments within individual superlayers and these segments are then linked together to form tracks across the three Regions within one sector. Due to the comparatively small size of the drift cells and the large number of wire layers, the track momenta can already be reconstructed with a resolution of 3% to 5%. Additional information on these tracks, derived from the Cherenkov, time-of-flight, and

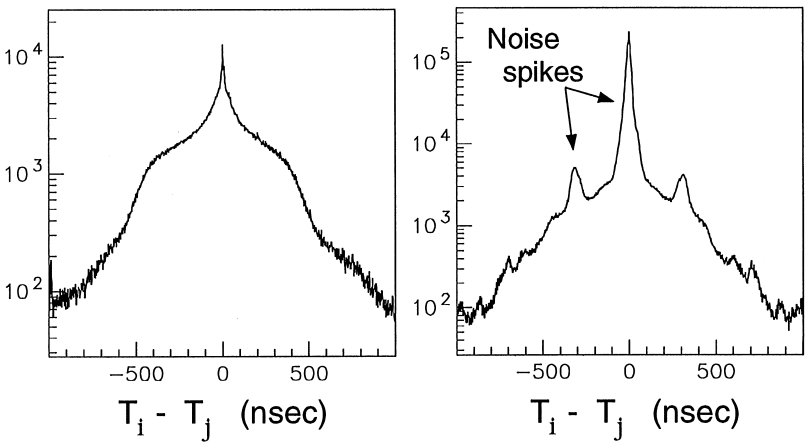

Fig. 24. Distribution of time differences between all pairs of hits from one contiguous group of 96 wires for two R2 chambers with different noise levels. The left plot corresponds to a chamber with much less noise than the chamber shown in the right plot, which has clear evidence of a coherent noise contribution.

electromagnetic calorimeter detectors, allows for determination of the identities and speeds of the charged particles. In the second stage of the analysis, flight-time information of the particles from the target to the outer scintillators is used to correct the measured drift times. A pre-determined table is then used to convert the corrected drift times to drift distances. These corrected track positions in each drift cell are fit in a procedure known as "time-based" tracking in order to determine the final track parameters.

The drift time is given by the following expression:

$$t_{\mathrm{drift}} = t_{\mathrm{start}} + t_0 - t_{\mathrm{TDC}} - t_{\mathrm{flight}} - t_{\mathrm{prop}} - t_{\mathrm{walk}} \quad (1)$$

where t_{start} is the event start time, t_0 is the fixed-time delay for the wire, t_{TDC} is the raw time measured by the TDC, t_{flight} is the flight time of the particle from the reaction vertex to the wire, t_{prop} is the signal propagation time along the wire, and t_{walk} is a time-walk correction made for short drift times due to different ionizations for slow and fast particles. Note that t_{TDC} is subtracted in the equation above because the TDCs are operated in common stop mode.

With photon beams the event start time is defined by coincident signals from the photon tagging system, an array of "start" counters surrounding the target (which replace the mini-torus during photon running), and the time-of-flight detectors. With an electron beam, the event start time is given by the time-of-flight counter time for the primary scattered electron corrected for the calculated flight time of this electron from the target.

Through the use of an appropriate function, the drift time determines the distance-of-closest-approach (DOCA) of the charged-particle track to the sense wire. However, there remains an ambiguity regarding which side of the sense wire the track passed by. This "left–right ambiguity" is resolved within the individual superlayers by comparing the χ^2 values for the track fit for all different combinations of drift-distance signs. After selection of the full set of drift-distance signs within each superlayer, a final fit results in improved track parameters.

7.2. Alignment procedures

As described in Section 3.4, each of the 18 drift chambers was surveyed after installation into CLAS. The survey procedures were different for each Region, and each method had drawbacks because of limited viewing angles. Additionally, the torus cryostat, which supports all of the chambers, moved slightly during installation due to the load of the detectors. For these reasons, the survey values for the chamber geometry were viewed only as a reasonable starting point to be refined by comparisons with data.

To adjust the chamber geometry parameters to improve the tracking resolution, "straight-track" data with the torus magnetic field off were analyzed. The results of this procedure indicated that the best-fit position of the chambers along the three coordinate axes varied by up to several millimeters relative to the surveyed positions. These studies of the absolute and relative chamber positioning are still ongoing, and should ultimately allow for the best-fit determination of more complex degrees of freedom such as chamber pitch, yaw, and roll. At this point, however, wire sag due to gravitational forces and chamber distortions, which enter at the level of several hundred microns in the worst case, have yet to be corrected for in the track reconstructions.

7.3. Time-delay calibration

As indicated in Eq. (1), the fixed-time delays for each wire must be known in order to determine the drift times. These delays, which derive mainly from cable lengths, were obtained using a Hewlett–Packard DG535 pulser to generate two pulses having a constant time separation. The first of these pulses was distributed to the 31 ADB crates; the second was sent to the trigger electronics in order to produce a common stop distributed to the TDCs. The average measured TDC value for each channel then provided the relative t_0 for each signal wire.

Synchronous delivery of the "start" signals to the Trigger Calibration Interface (TCI) boards in each ADB crate (see Section 4.3.1) was ensured by using cables of equal length and identical electronic components. On the TCI boards the start signal was

switched pulse-to-pulse, and either routed back to the on-chamber electronics through an additional twisted pair in the signal cable, or else sent directly into the TDCs. Accordingly, for every drift-cell channel two TDC values were read out, one for the direct pulse into the ADB, and the other for the pulse sent to the chamber electronics. The time difference of these signals yields twice the delay due to cable length; the sum of the times measures the delay from both cables and electronics plus one constant time offset between the trigger electronics and the drift-chamber TDCs.

7.4. Time-to-distance calibration

Each hit on a track is characterized by two parameters, the measured drift time from the sense wire and the distance-of-closest-approach (DOCA) to the sense wire. A best fit to the dependence of DOCA on time defines the drift-velocity function of the drift cells. However, several factors complicate this analysis. For example, the DOCAs obtained from the fitted tracks are biased quantities since an initial estimate of the drift-velocity function is used in the track determination. Moreover, the drift cells are not circular, as the analysis implicitly assumes, but are hexagonal, leading to angle-dependent corrections. The R2 chambers, in particular, are in a region of high and spatially varying magnetic field. Finally, the different ionization densities of the tracks from particles with different velocities leads to substantial time-walk corrections for tracks near the wire. Each of these points is briefly discussed in this section.

The effect of the DOCA bias was reduced by fitting data from a selected single layer in each superlayer that was excluded from the original track fit. However, excluding a layer from the track fit is not enough to entirely eliminate all bias. Because of the regular brick-wall cell layout, tracks at entrance angles of 0° or 30° yield biased values for DOCA, even from the excluded layer, because the times in the included layers are strongly correlated with the value of the time in the excluded layer.

Fig. 25 shows the isochrone contours and electric-field lines for a representative R3 and R2 cell. Note that the contours are circular close to the wire but become hexagonal near the outer boundaries of the cell. This illustrates the necessity of knowing the entry angle of the track in order to determine the drift distance to the sense wire from the measured drift time.

7.4.1. Function parameterization

The drift time to drift distance function for R3 at a given track entrance angle is parameterized in

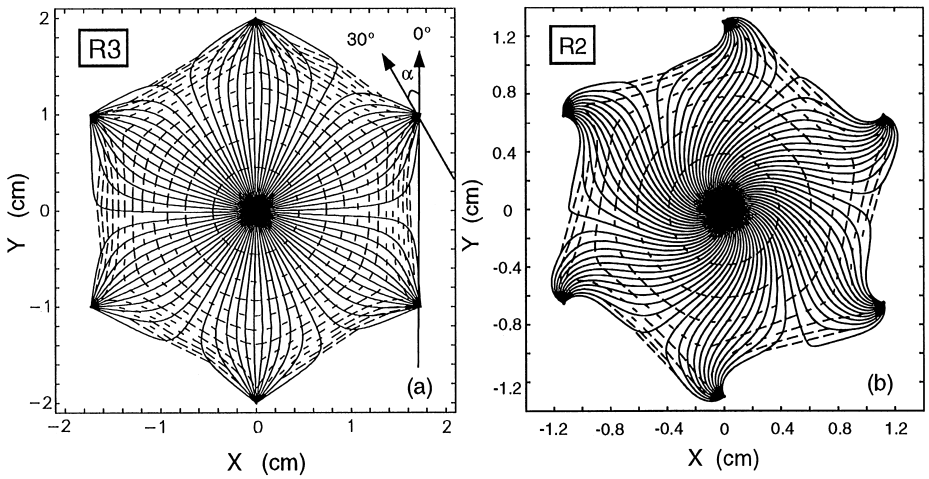

Fig. 25. Plot of electric-field lines and equal-time isochrone contours (100 ns interval) for a 90% argon – 10% CO_2 gas mixture for (a) an R3 drift cell where two rays are drawn highlighting two different track entrance angles of $\alpha = 0^\circ$ and 30°, and (b) and R2 cell that was assumed to be located within a uniform 1 T magnetic field along the z direction.

terms of a power law [22] as

$$x(t) = v_0 t + \eta\left(\frac{t}{t_{\max}}\right)^p + \kappa\left(\frac{t}{t_{\max}}\right)^q \quad (2)$$

where v_0 is the value of the saturated drift velocity near $t = 0$, and the coefficients η and κ, and the exponents p and q, are determined by fitting the time-to-distance correlation. Polynomial forms give comparable results and, in fact, are used for R1 and R2.

Inspection of Fig. 25a reveals that for tracks near the outer edge of the cell, the first arriving ions follow the electric-field line from the field wire to the sense wire, independent of track entrance angle. Their corresponding drift time is referred to as $t_{\max}$. A reduced or normalized drift time $\hat{t} = t/t_{\max}$ is used as an argument of the time-to-distance function that satisfies the cell boundary constraint,

$$x(\hat{t} = 1, \alpha) = C\cos(30^\circ - \alpha). \quad (3)$$

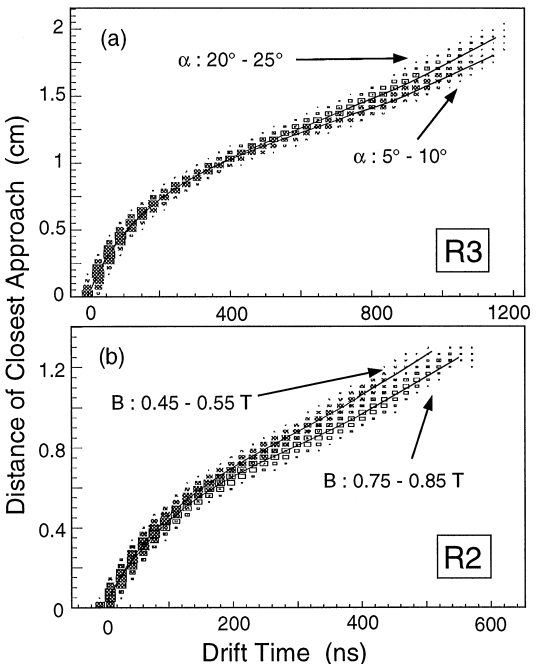

Fig. 26. Scatterplot of DOCA versus the corrected drift time for (a) R3 axial wires showing the track local-angle dependence, and (b) R2 axial wires showing the magnetic-field dependence where the local angle range is between 23° and 25°. The overlaid curves represent the fitted time-to-distance function.

The angle α is the track entrance angle and C represents the cell size. At any given entrance angle, as shown in Fig. 26a, the time-to-distance function can be deduced using a correction function $f(\hat{t})$:

$$x(\hat{t}, \alpha) = x_0(\hat{t}, \alpha_0) + C(\cos(30^\circ - \alpha) - \cos(30^\circ - \alpha_0))f(\hat{t}). \quad (4)$$

In this expression, x_0 represents the drift distance expected for a given normalized drift time assuming an entrance angle α_0. This entrance angle represents the average entrance angle for the full fitted data sample. The function $f(\hat{t})$ is used to correct the extracted drift distance for the true entrance angle of the track.

Since the R2 chambers are located between the torus cryostats, the inhomogeneous magnetic field affects the drift velocity as shown in Fig. 26b. In particular, the field rotates and shrinks the isochrones as shown in Fig. 25b. These effects can be modeled by a modification to the effective entrance angle of the track and by an increase in $t_{\max}$. Both of these corrections are assumed to depend only on the magnitude of the magnetic field, and not its direction, following a study described in Ref. [23].

The rotation of the isochrones is parameterized as a shift in the effective entrance angle. This correction term α_c is determined from a GARFIELD simulation to be

$$\alpha_c = \cos^{-1}(1 - aB) \quad (5)$$

where a is a constant and B is the magnetic field strength.

The maximum drift time used in the time-to-distance function was extracted directly from the data. For R2 the maximum drift time was parameterized as

$$t_{\max}(B) = t_{\max}(0) + bB^2 \quad (6)$$

where b is a constant and B is the magnetic field strength.

At any given local magnetic field point, the time-to-distance function included an additional linear correction term $\beta(\hat{t})$ to describe the magnetic field dependence [24]

$$x(\hat{t}, \alpha, B) = x(\hat{t}, \alpha - \alpha_c, B_0) + (B - B_0)\beta(\hat{t}). \quad (7)$$

In this expression, B_0 represents the average magnetic field value for the full fitted data sample. For the R1 and R3 functions, no magnetic field dependence is included, as the chambers are located outside the torus cryostats in regions that are relatively field-free.

7.4.2. Laser calibration system

Electron drift velocities in the chambers can fluctuate by up to 20% due to changes in pressure, temperature, and gas mixture. If not taken into account, such changes can substantially degrade the chamber resolution. The drift velocities can be monitored by measuring t_{max} directly. This can be done by producing photoelectrons at the field wire with a pulsed ultraviolet beam from an N_2 laser [22]. These measurements are made in three calibration chambers that reproduce the cell dimensions of the different Regions. Each contains a central hexagonal drift cell surrounded by six other drift cells. The results of GARFIELD calculations indicated that the properties of the central cell in this configuration were almost identical to those of a single cell in an infinite lattice.

The three calibration chambers are mounted side-by-side together with a Laser Photonics LN203C laser inside a Faraday shield. The laser pulses have an energy of 0.125 J and a FWHM of 0.8 ns. Each chamber is attached to a base that serves to align it relative to the beam, and also to tilt it so that the struck field wire is not shadowed by neighboring field wires. The beam is finally stopped by a fast photodiode that provides the start signal for the drift-time measurements. The stop signal is derived from the sense-wire signal of the central drift cell.

Measurements of t_{max} are typically made at half-hour intervals. A fraction of the gas returning from the chambers is diverted through the calibration chambers, whose pressures and temperatures are matched to the corresponding values in the hall. A feature of the typical results shown in Fig. 27 are the abrupt changes observed in the R3 values for t_{max}. These changes, which correspond to days of high humidity, appear to originate from the permeability of the gas windows to water vapor and the subsequent condensation of the vapor at night and re-evaporation by day in the gas-system buffer tanks. The gas supplied to CLAS was essentially water-free, whereas the return gas contained water vapor at the level of a few tenths of 1%. Even ignoring the anomalous day/night variations in t_{max}, the data show up to 10% changes in the maximum drift time over a one- to two-day period.

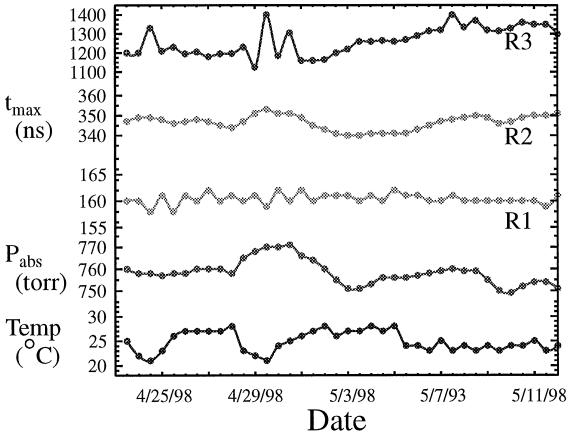

Fig. 27. Results from the laser-calibration system for a 90% argon – 10% CO_2 gas mixture during a 19-d period.

Since there is no capability for applying magnetic fields to the R2 calibration chamber, the values measured for t_{max} have to be corrected prior to being used for monitoring. The correction factors determined using GARFIELD are $\approx 30\%$.

8. System performance

8.1. Chamber lifetime

In order to satisfy the statistical requirements of the experimental program, a critical design goal for CLAS is the ability to make routine measurements with electron beams giving luminosities of up to 1×10^{34} cm^{-2} s^{-1}. The tolerable luminosity in CLAS is generally set by the large flux of Møller electrons and low-energy photons produced from the targets by the multi-GeV incident electron beam. This constraint is severe for the drift chambers since they are close to the target. Particularly for the R1 chambers, the large flux of particles limits the luminosity in two ways. First, a large

number of background-related hits in the chambers makes track reconstruction very difficult. The working assumption is that the analysis software can tolerate no more that a 5% accidental chamber occupancy in order to successfully reconstruct charged-particle tracks. Second, the effects of sustained high luminosities are unfavorable for long chamber lifetimes. Aging correlates directly with the current carried by the chambers, maximum values for which have been set following detailed studies with electron beams [25].

The useful chamber lifetime is difficult to predict, as it depends on many different parameters such as construction materials, purity of the operating gas, chamber geometry, and other unknown effects. Fig. 28 shows the R1 chamber lifetime, defined in terms of accumulated charge, as a function of angle. These estimates are based on the currents drawn from the HVTBs at a luminosity of 1×10^{34} cm^{-2} s^{-1}. The lifetime will be shortest for small angles where the flux of charged particles is largest. The lifetime estimate presented in Fig. 28 pessimistically assumes that the chambers are continuously illuminated. In practice, the actual lifetime will likely be at least five times longer, and that for the outer drift chambers should be about an order of magnitude longer as they see much reduced ionization relative to R1.

Fig. 29 shows the average currents drawn by the R1 drift cells as a function of the current in the mini-torus. By confining the expansion of the flux

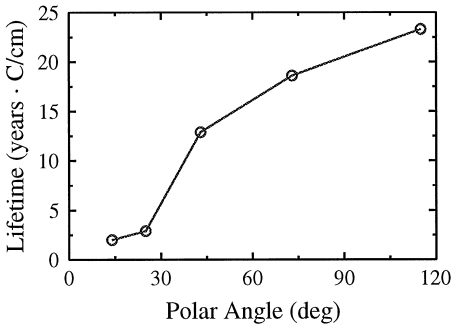

Fig. 28. Estimated R1 chamber operating lifetime in years times C/cm of charge accumulated as a function of the average polar angle spanned by each of the HVTBs. Data are shown with the mini-torus at full field, and assume continuous operation of the chamber at a luminosity of 1×10^{34} cm^{-2}s^{-1}.

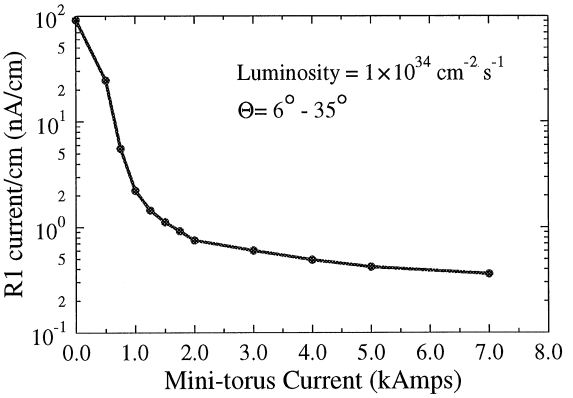

Fig. 29. Measurement of R1 sense-wire current per cm of wire length as a function of the mini-torus current at design luminosity for the most forward angle wires.

of Møller electrons, this magnet reduces the chamber currents by several orders of magnitude.

8.2. Missing channels

During two years of operational experience with CLAS, drift cells have failed for reasons that include broken sense wires and other hardware problems, bad SIPs, unplugged signal cables, and electronics failures in the ADB and MUX boards. The breakdown of these faults in each Region is shown in Fig. 30.

When a wire breaks during a run period, the affected region is electrically isolated by turning off the high voltage for the minimum number of surrounding drift cells, and the run is continued. Broken wires are removed during maintenance periods, and the high voltage is restored.

8.3. Efficiency

The chamber efficiency can be described in terms of either the "layer efficiency" or the "tracking efficiency". The layer efficiency is the probability that a good hit is recorded in a wire layer through which the track has passed, based on the evidence from all other layers in the superlayer. This is called the "excluded-layer method". The layer efficiency is a measure of the intrinsic drift cell efficiency for the particular choice of gas mixture, high-voltage set point, and discriminator level.

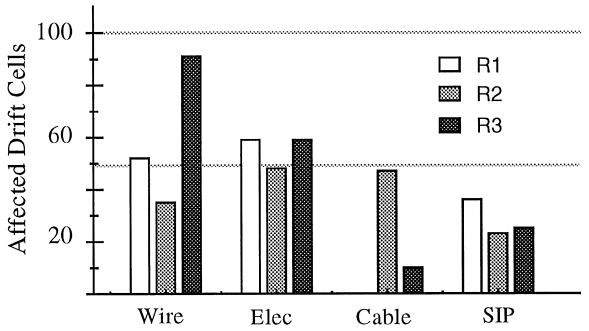

Fig. 30. Accounting for all of the drift chamber isolated missing drift cells for each of the different Regions. This list includes sense wires removed from the system (Wire), bad electronics channels (Elec), unplugged signal cables (Cable), and bad SIPs (SIP).

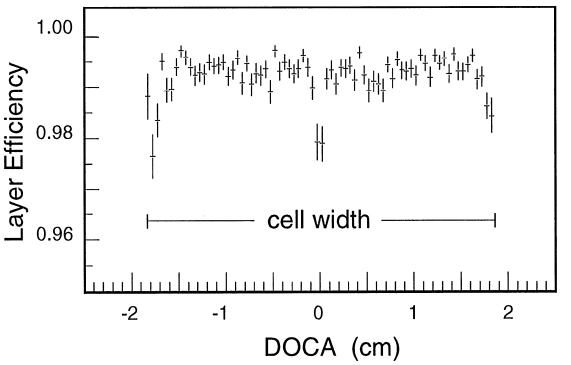

Fig. 31. The layer efficiency plotted versus the distance-of-closest-approach (DOCA) to a sense wire. This typical sample is from an R3 sector.

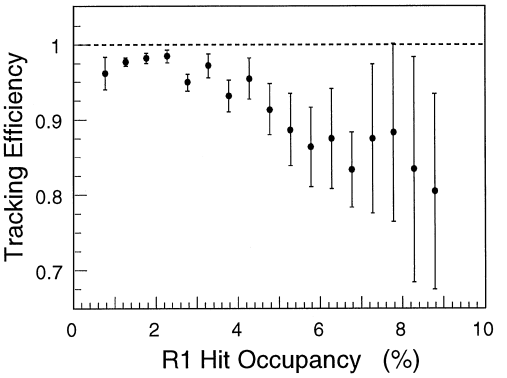

Fig. 32. Tracking efficiency plotted as a function of the R1 hit occupancy (%) for recoil protons from elastic scattering where the corresponding electron track has been reconstructed.

The plateau curves used to set the high-voltage operating points for the chambers show that the average layer efficiency is $> 98\%$ (see Fig. 20). Fig. 31 reveals that a large contribution to the 2% inefficiency comes from tracks that pass close to the sense wire. These tracks give rise to signals that have low pulse height and long duration, and thus may escape detection.

The tracking efficiency is the probability of identifying a track when, based on kinematics, a charged particle is projected to pass through the active region of the drift chambers. For example, such a particle would be a recoil proton from e–p elastic scattering. Fig. 32 shows the calculated tracking efficiency for recoil protons from e–p elastic scattering, plotted as a function of the R1 hit occupancy for the sector where the recoil proton is expected. The tracking efficiency remains $> 95\%$ for chamber hit occupancies up to 4%. At higher occupancies the tracking efficiency begins to fall off.

8.4. Track resolution

The tracking resolution is the spread in the reconstructed momenta and angles of the charged-particle tracks relative to their true values. These tracking uncertainties arise from three primary sources: multiple scattering in the material along the particle trajectory, geometric misalignments of the separate tracking chambers or lack of knowledge of the true value of the traversed magnetic field strength, and finally, the single-wire resolution.

Fig. 33 is an illustration of the effect of finite track resolution on the reconstruction of the beam–target vertex. The reconstructed beam vertex position is plotted versus the dimension along the beam line for data with the beam incident upon an empty target cell. These data were acquired for charged tracks in the angular range from 75° to 105°. The peaks at the z-positions – 2.0 and 1.8 cm – correspond to the entrance and exit windows of the 3.8-cm long target, and the peak at $z = 3.8$ cm corresponds to a 20-μm aluminum calibration foil.

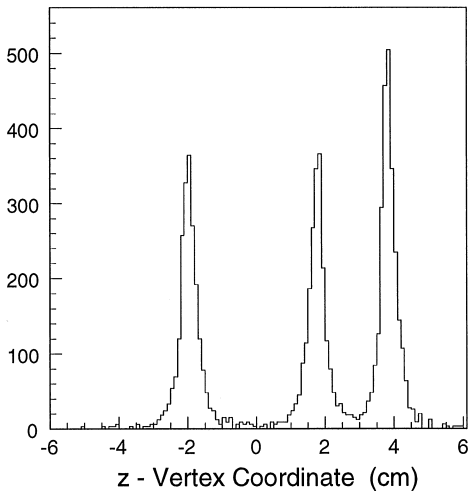

Fig. 33. Reconstructed beam–target vertex position for an electron beam incident upon an empty target cell. The three peaks correspond to the target entrance and exit windows and an aluminum calibration foil.

The width of each peak is about $\sigma = 2$ mm. As the R1 wires illuminated in this reconstruction are about 0.5 m from the target, this peak width roughly translates into an angular uncertainty at the position of R1 of about 4 mrad. Again, this resolution includes contributions from the intrinsic system resolution, chamber misalignment and magnetic field uncertainties and multiple scattering.

As a consistency check, Fig. 34 shows for one sector the mass distribution of the hadronic final state W for 2.4 and 4.0 GeV e–p scattering. The elastic-peak width ($\sigma_{2.4} \approx 12$ MeV, $\sigma_{4.0} \approx 16$ MeV) provides a measure of the mass resolution of the tracking system. The part of the mass resolution arising from spatial resolution of the tracking chambers is expected to grow with increasing momentum; thus the elastic peak widths at 2.4 and 4.0 GeV are consistent.

The various contributions to the overall system resolution can be studied through detailed detector simulations as well as CLAS data. For the overall track fit through a given sector, an additional uncertainty of 300 μm for R1, 400 μm for R2, and 450 μm for R3 is added in quadrature to the measured single-wire resolution (see next sub-section) to account for chamber misalignments, uncertainties in the CLAS magnetic field, and multiple scattering. The final χ^2 distribution is shown in Fig. 35 for the full fit through all six superlayers of each sector.

8.5. Chamber resolution

The intrinsic chamber resolution, or single-wire resolution, is a measure of the uncertainty between the DOCA of the track and the distance as calculated from the time of the wire hit. The

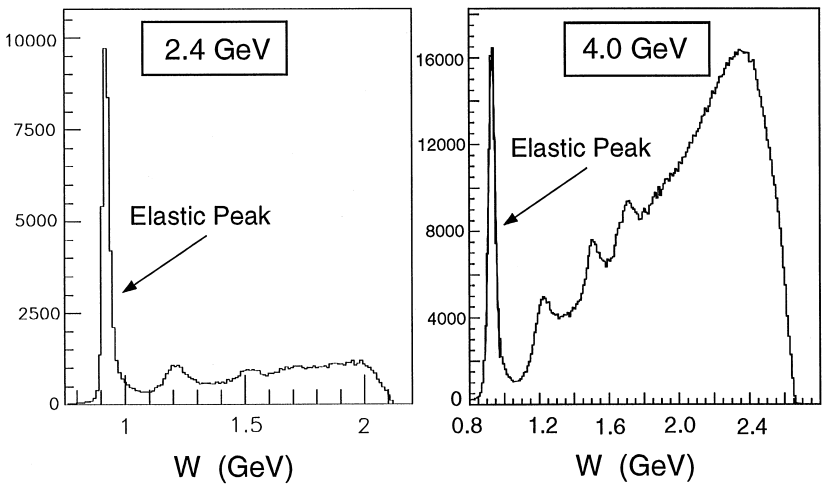

Fig. 34. Reconstructed 2.4 (left) and 4 GeV (right) W distribution for one sector showing the e–p elastic peak and inelastic excitations.

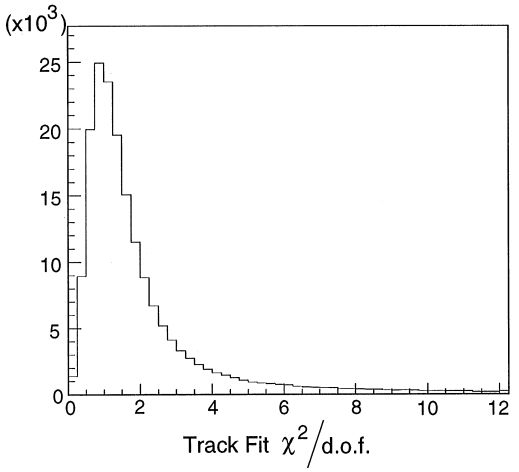

Fig. 35. χ^2 distribution per degree of freedom of the overall track fit using the residual sigmas for each of the drift chamber Regions and an additional error to account for chamber misalignments and imperfections of the magnetic-fiels maps.

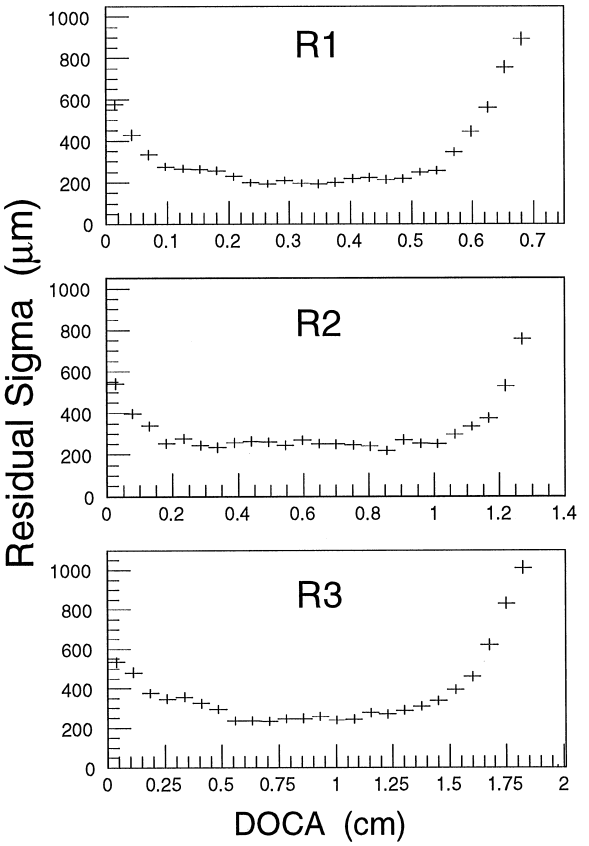

Fig. 36. Track-hit residual sigmas plotted versus the fitted DOCA for each of the three drift chamber Regions.

excluded-layer fitting method has been used to estimate the single-wire resolution within a given superlayer. Tracks fitted to all hits except those on the excluded layer are projected to determine the intercept in the excluded layer. The fit residual is the difference between the fitted DOCA of the track and the value of DOCA as calculated from the time of the hit in the excluded layer. The variance of this residual distribution is the quadratic sum of the single-wire resolution and the track position uncertainty at the excluded layer. This variance overestimates the single-wire resolution. Since there are six layers per superlayer and layer 3 is excluded from the fit, this amounts to a 10–15% over-estimate.

Fig. 36 shows the width of the track-hit residual distribution plotted versus DOCA for each of the different chamber Regions. The single-wire resolution worsens near the wire and also at the outer edge of the cell. This arises due to finite cluster sizes due to the Poisson distribution of ion-pair production along the path of the primary ion near the sense wire along with time walk effects and the divergent nature of the electric field lines near the field wire. The average single-wire resolution in the middle portion of the cell for each Region is presently about 200 to 250 μm. The whole-cell average is about 310, 315 or 380 μm for R1, R2, and R3, respectively.

9. Conclusions

The toroidal geometry of the CLAS spectrometer necessitated a particle-tracking system of unconventional design. Design challenges and solutions include the following:

- The necessity to conceal inactive areas of the drift chambers within the shadow regions of the torus cryostat resulted in very thin endplates and low-profile wire connection schemes and on-board preamplifiers.

- The toroidal shape of the magnet and the desire to have measurements before, within, and after the high-field region, resulted in the design and fabrication of nested multi-layer drift chambers that have cylindrical profiles.
- The fabrication of chambers that support large static wire tensions, but have thin endplates necessitated three novel support systems: the "six chambers as a unit" design of R1, the spring mounting to the cryostat of R2, and the thin outer carbon shell of R3.
- The need for precise tracking in a system with non-saturated drift velocity (necessitated by the requirements of large drift distances, non-flammable gas mixtures and low-gain operation) resulted in a semi-automated calibration and monitoring software package.

The CLAS drift chamber system has been in routine operation since January 1998. The system has reached its design goals of high-luminosity operation (1×10^{34} cm^{-2} s^{-1}) in a high-flux electromagnetic reaction environment, with very good track reconstruction efficiency over a large range of angles and magnetic fields. The single-wire efficiency is greater than 98% and the single-wire resolution is about 330 μm averaged over all drift distances and all 18 chambers, with each chamber showing a characteristic 250 μm resolution in the cell center.

Acknowledgements

The authors wish to thank the crews of wire stringers and technicians who participated during the sector construction at the University of Pittsburgh, Old Dominion University, and Jefferson Laboratory, as well as the support of the technicians involved with installation of the detectors into CLAS. The authors also thank S. Corneliussen for his careful reading of the draft. This work was supported in part by DOE contract DE-AC05-84ER40150, DOE grants DE-FG02-87ER40315, DE-FG05-94ER40859, DE-FG02-96ER40960, DE-FG02-96ER40980, and NSF grant NSF-PHY-9412479.

References

[1] CEBAF Hall B Conceptual Design Report, 1990.
[2] M.D. Mestayer, Choosing the correct combination of sense, field, and guard wire voltage CLAS-Note 92-005, 1992.
[3] J.A. Kadyk, Nucl. Instr. and Meth. A 300 (1991) 436.
[4] S.B. Christo, M.D. Mestayer, Minimizing cathode emission in drift chambers, CLAS-Note 92–016, 1992.
[5] W. Campbell, J. Scialdone, Outgassing data for selecting spacecraft materials, NASA Internal Report RP-1124 Rev. 3, 1993.
[6] S.B. Christo, Considerations for crimping the CLAS drift chamber wires CLAS-Note 89-021, 1989.
[7] D.S. Carman et al., Nucl. Instr. and Meth. A 419 (1998) 315.
[8] R.A. Schumacher, R. Magahiz, The region 1 drift chamber endplates: procurement history and inspection results, CLAS-Note 94-018, 1994.
[9] S.J. Bianculli, Master's Thesis, University of Pittsburgh, 1993.
[10] R.A. Thompson et al., Issues in stringing the CEBAF large acceptance spectrometer region 1 drift chamber, CLAS-Note 96-019, 1996.
[11] S. Bernreuther et al., Nucl. Instr. and Meth. A 367 (1995) 96.
[12] W.L. Imhof et al., Space Sci. Rev. 71 (1995) 305.
[13] R. Bouclier et al., Nucl. Instr. and Meth. A 350 (1994) 464.
[14] L.M. Qin et al., Nucl. Instr. and Meth. A 411 (1998) 265.
[15] M. Chew et al., Investigations into wire sag in the CLAS drift chambers, CLAS-Notes 89-016, 89-017, 1989.
[16] S.A. Roth, R.A. Schumacher, Nucl. Instr. and Meth. A 369 (1996) 215.
[17] R.A. Schumacher, Region one drift chamber analysis of survey data, CLAS-Note 98-001, 1998.
[18] F.J. Barbosa, A preamp for the CLAS DC, CLAS-Note 92-003, 1992.
[19] M.F. Vineyard, T.J. Carroll, M.N. Lack, in: M. Crowley-Milling, P. Lucas, P. Schoessow (Eds.), Proceedings of the 1995 International Conference on Accelerator and Large Experimental Physics Control Systems, Fermilab Report CONF-96/069, W-PO-37, 1996.
[20] GARFIELD has been developed at the University of Mainz by R. Veenhof and revised by M. Guckes and K. Peters. See HELIOS-note 154, 1986.
[21] D.S. Carman, CLAS region I prototype detector, CLAS-Note 96-022, 1996.
[22] M.D. Mestayer et al., Nucl. Instr. and Meth. A 367 (1995) 316.
[23] M.D. Mestayer et al., IEEE Trans. Nucl. Sci. NS-39 (4) (1992) 690.
[24] L.M. Qin et al., Performance of a region II drift chamber prototype and region II drift chamber tracking, CLAS-Note 96-018, 1996.
[25] D.S. Carman et al., Hall B test run: drift chamber studies, CLAS-Note 97-001, 1997.